NTNU

Norwegian University of
Science and Technology

Wave Energy Conversion

Simulation Verification and Linearization of Direct Drive Wave Energy Converter with Variable DC-link Voltage Control

Arne Marius Ditlefsen

Master of Science in Energy and Environment

Submission date: June 2009

Supervisor: Tom F. Nestli, ELKRAFT

Co-supervisor: Jonas Bakken, Fred Olsen Ltd.

Norwegian University of Science and Technology
Department of Electrical Power Engineering

Problem Description

The world first commercial wave farm was launched in Portugal in 2007.
In other parts of the world WEC (Wave Energy Converter) devices are at R&D and prototype stages, many with promising prospective. All electric power take off systems are in focus and several possible solutions can be found in the literature. The task of this project will be to investigate one such solution: A Permanent Magnet Synchronous Generator feeding into a 6-pulse diode rectifier with variable DC link voltage.
The task is divided in three parts.

1. Implement a model of the WEC system in Matlab and develop and demonstrate stable control that emulates passive loading of the generator.

2. Verify simulation results by laboratory experiments.

3. Make a linearization of the system that can easily be adapted to any scale and rating.

Assignment given: 19. January 2009
Supervisor: Tom F. Nestli, ELKRAFT

Abstract

Lowering the cost of wave energy conversion is an essential task for it to succeed as a future energy resource. In this work a converter, assumed cheaper than the regular back to back converter setting, have been investigated for a electric direct drive point absorber. Both experimental work and simulations are used in the analysis. In the experimental work, a permanent magnet generator with a 6-pulse diode rectifier, a DC-link and a DC/DC converter equivalent, was used. Steady state, dynamic and transient measurements were preformed and a simulation model was compared to the measurements. Good results were obtained and deviations were in general small, mostly $\pm$ 3% for voltage and current measurements and $\pm$ 8 % for torque measurements. Based on transient measurements and simulations a general linearization of the system was made in order to obtain useful information about the system.

A step up converter was used in the simulation and it demonstrated stable passive loading control. By using the information obtained by the linearization, the performance of the simulation model was improved by decreasing the DC-link capacitance. The modified simulation model had significant less torque ripple than the initial. The linearization model also can been used to identify time delay represented by the power take off unit in a wave energy converter. This will be done for a commercial size wave energy converter summer 2009.

Contents

List of Tables

List of Figures

Acronyms

PTO - Power take off untit

WEC - Wave energy converter

PMG - Permanent magnet generator

RPM - Rounds per minute

CCM - Continous coduction mode

DCM - Discontinous conduction mode

1 Introduction

The worlds demand for energy is rapidly increasing. It is indicated that it will almost triple by 2050 and oil can only supply the world for up to 150 years more[1]. Renewable energy has great potential, but the cost of installation and operation can not compete with conventional gas, coal and nuclear power. Especially wave energy has a long way to go. Governmental subsidies are necessary to make the transition to renewable energy production. In Portugal subsidies on the electricity tariff has resulted in the first commercial wave energy power plant[2]. A necessary strategy to better the economic payoff from wave energy is by active control. With active control is the power take off (PTO) machinery used to manipulate the behaviour of the wave energy converter (WEC) in such a way that the energy output is maximized[3]. There are several ways to implement active control; with hydraulics, pneumatics or with direct drive electric generators.

There are also several concepts of converting the kinetic energy in the waves to mechanical energy in the WEC. Oscillating water column, overtopping devices and point absorbers are the main concepts[4]. The background for this work is the Fred Olsen FO3 project. They have been working on the point absorber concept with different types of PTO. A promising PTO system is the direct electric drive. That is the reason why the point absorber with direct electric drive is the starting point of this work. There are several ways to implement such a system and the most effective and cost efficient is yet undiscovered. Figure 1.1 shows a schematic setup of the selected concept on the left and a picture of the Fred Olsen point absorber rig (FO-rig) on the right.

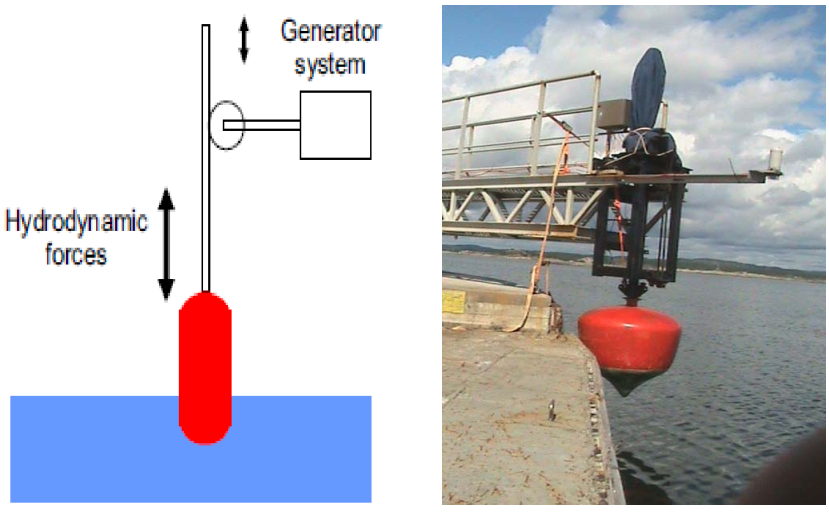

Figure 1.1: Point absorber with direct electric drive schematic and picture.

An all electric PTO system with regular back to back converter [5] have already been investigated by FO3 with good results, but a more cost effective solution is desirable. This work will therefore investigate the FO-rig with a new converter setting which probably is more cost effective. Economical considerations will not be part of the work, as it is assumed that such a solution is cheaper, but some thoughts on the topic will be mentioned in the discussion.

A project work has already been preformed on the topic and an idea for such a system has been implemented in a simulation model. It turned out that some of the choices done were weak e.g. selection of converter type and DC-link capacitance. The main challenge encountered was torque fulutuations due to large ripple in current. This work will therefore coop with these tasks. Some of the results found during the project are still used in this work which is mainly divided in two parts: One with experimental work and one with simulations in MATLAB/Simulink. For the experimental work a simulation model of the system will be verified by measurements in the lab. A generalized linearization is to be made based on the experimental results, and will hopefully contribute with useful information about the system. In the simulation part wave data from the FO-rig tests will be used to emulate stable passive loading control of the converter system.

2 Theory

2.1 Diode rectifier

This subsection covers the basics of diode rectification and the information is from power electronics[6].

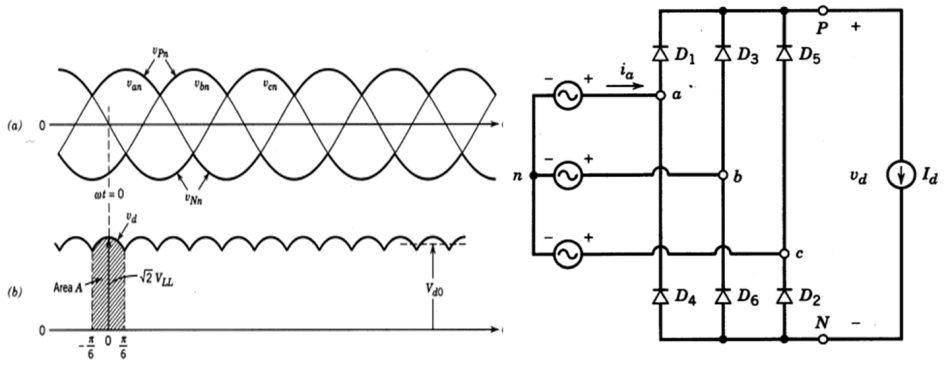

Figure 2.1.1: Left:a)Phase voltages b)Output voltage vaweform. Right: Circuit diagram of diode rectifier with constant DC-side current.

By looking at figure 2.1.1 the expression for the mean DC-side voltage of a three phase diode rectifier, V_{d0}, can be calculated as in equation 2.1.1.

$$V_{dO} = \frac{1}{\frac{\pi}{3}} \int_{-\frac{\pi}{6}}^{\frac{\pi}{6}} \sqrt{2} V_{LL} \cos(\omega t) d(\omega t) = \frac{1}{\frac{\pi}{3}} \sqrt{2} V_{LL} = 1.35 V_{LL} \qquad (2.1.1)$$

Permanent magnet generators have inductance in their phase windings. This will lead to voltage loss during current commutation since inductance make instantaneous commutation impossible. A figure of current commutation from diode five to one and the respective waveforms are illustrated in figure 2.1.2.

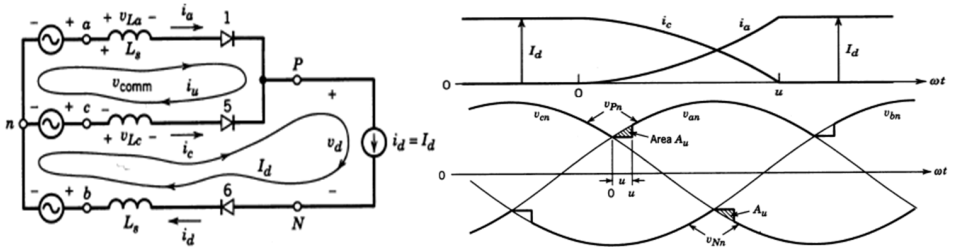

Figure 2.1.2: Current commutation with inductance in the rectifier circuit.

The area A_u can be expressed as $\omega L_s I_d$ and is the voltage "lost" every $\frac{\pi}{3}$.The average DC-side voltage can then be calculated as in equation 2.1.2:

$$V_d = V_{do} - \frac{\pi}{3}\omega L_s I_d = 1.35 V_{LL} - \frac{\pi}{3}\omega L_s I_d \tag{2.1.2}$$

It is desirable to express the generator resistance and inductance as a DC-equivalent. Two phases are conducting at any time when using a diode rectifier and the effective resistance and inductance is therefore 2 times the phase quantities. Under commutation are the quantities 1.5 because of paralleling of two phases. Commutation time depend on the choice of diodes and is usually short enough to neglected[7].

$$R_{eq} = 2 \cdot R_g \tag{2.1.3}$$

$$L_{eq} = 2 \cdot L_g \tag{2.1.4}$$

The relation between phase current and DC-side current, I_d, in the idealized case is given in equation 2.1.5.

$$I_{phase} = 0.816 I_d \tag{2.1.5}$$

2.2 Permanent magnet generator

The permanent magnet generator (PMG) used in this work is a 3-phase generator with sinusoidal distributed windings. In the simulations it is modelled in the dq-reference frame with rotor flux linkage space vector as reference [16]. The dynamical behaviour of such a generator is given in equations 2.2.1, 2.2.2 and 2.2.3 .

$$\frac{d}{dt}i_d = \frac{1}{L}v_d - \frac{R}{L}i_d + p\omega_r i_q \tag{2.2.1}$$

$$\frac{d}{dt}i_q = \frac{1}{L}v_q - \frac{R}{L}i_q + pw_r i_d - \frac{\lambda p\omega_r}{L} \tag{2.2.2}$$

$$T_{em} = \frac{3}{2}p\lambda i_q + (L_d - L_q)i_q i_d \tag{2.2.3}$$

Where $L = L_d = L_q$ is the inductance of the d and q-axis windings, R is the resistance of the stator windings, i_d and i_q are the d and q-axis currents. v_d and v_q are the d and q-axis voltages, ω_r is the angular velocity of the rotor, λ is the amplitude of the flux linkage established by the rotor magnets, p is the number of pole pairs and T_{em} is the electromagnetic torque. In a round rotor machine with exterior mountned magnets is $L = L_q = L_d$, and the saliency term of the electromagnetic torque becomes 0. The realtion between i_q and DC-current was examined in the project work, and they were practically equal. The DC-current is therefore proportional to torque, as will be used during through this work.

Phase quanteties are also used; in this work open circuit induced voltage, E_a, is defined as:

$$E_a = \omega_{mech} \cdot \frac{k_E}{\sqrt{2}} \tag{2.2.4}$$

Where E_a is the generators open circuit line to line induced voltage in RMS. ω_{mech} is the mechanical speed of the shaft in RPM. k_E is the peak to peak voltage induced pr. RPM. The reason for choosing peak to peak voltage for k_E is because that is done in the datasheet of the generator B. The relation between ω_{mech} and $\omega_{electric}$ is given in equation 2.2.5 and 2.2.6.

$$\omega_{electric} Hz = \frac{1}{60}\frac{p}{2}\omega_{mech} \tag{2.2.5}$$

$$\omega_{electric}\frac{rad}{s} = \frac{\pi}{30}\frac{p}{2}\omega_{mech} \tag{2.2.6}$$

Where p is the polenumber of the generator.

2.3 Step up converter

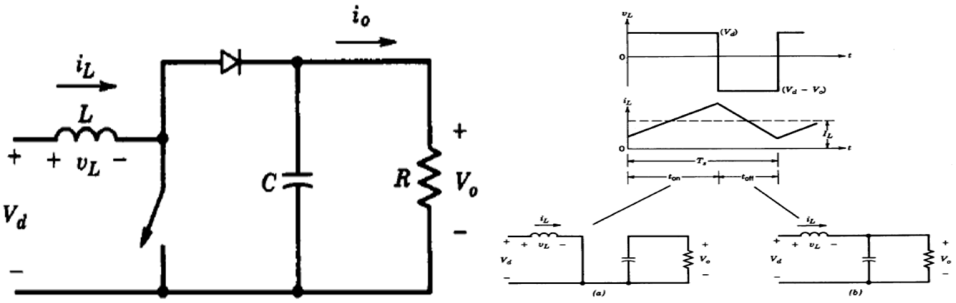

Figure 2.3.1: Left: Circuit diagram of step up converter. Right: CCM Step up converter, on and off states, and resulting waveforms.

The converter in figure 2.3.1 is working in steady state and in continuous conduction mode (CCM). It implies that the voltage integral across one period of T_s is zero and that the inductor current do not reach zero. When evaluating this integral the voltage ratio can be obtained as in equation 2.3.1:

$$V_d t_{on} + (V_d - V_0) t_{off} = 0$$

Keeping in mind that duty cycle, D, is $\frac{t_{on}}{Ts}$ and 1-D is $\frac{t_{off}}{Ts}$, voltage ratio can be obtained by dividing by T_s:

$$\frac{V_0}{V_d} = \frac{1}{1-D} \tag{2.3.1}$$

Given the voltage conversion ratio it can be observed that it is a step up converter because a duty cycle of 0 gives the same input and output voltage, and a duty cycle of 1 gives infinity output voltage. This is of course for a theoretical, ideal converter and for a practical converter this is not the case. Due to parasitic elements as inductor copper loss, the conversion ratio will have a maximum point for a certain D and increasing the duty cycle beyond this limit will cause the ratio to decrease. It is therefore important not allowing the duty ratio of the converter used in simulations to be higher than a maximum limit of approximately 0.8-0.9 [8].

Example of conversion ratio vs. duty cycle is given in top left of figure 2.3.2

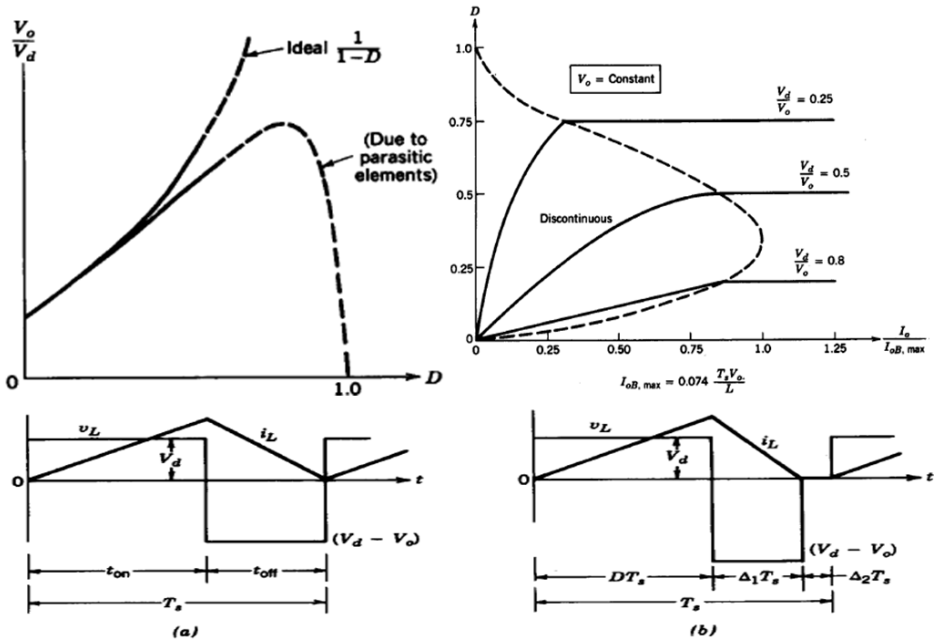

Figure 2.3.2: Top left: conversion ratio as functon of duty cycle. Top right: Boundary between CCM and DCM with constant V_0. Bottom: Boundary between CCM and DCM(Left) and DCM(Right) waveforms.

If the inductor current reaches zero during one interval, T_s, is the converter working in discontinuous conduction mode (DCM) as shown on bottom right in figure 2.3.2. Another interval with zero inductor current is then added, indicated $\Delta_2 T_s$ in the figure. It is not desirable to have a converter working in DCM because of bad switch utilization. The energy transfer through the converter will the have to be executed in a shorter amount of time and the peak currents will be higher than necessary. Ripple in capacitor voltage assuming a constant current can be expressed as:

$$\Delta V = \frac{\Delta Q}{C} = \frac{IDT_s}{C} \tag{2.3.2}$$

2.4 Passive loading

Passive loading is done by applying a generator torque that is proportional to shaft speed of the generator as in equation 2.4.1.

$$T_{em} = B_{damp} \cdot \omega_{mech} \tag{2.4.1}$$

Where T_{em} is the electromechanic torque of the generator and B_{damp} is referred to as the damping constant. An ideal converter working with passive loading control can be represented as a resistor. This can be explained by a simplified generator model were the generator inductance and resistance are neglected. $I_{gen} = k_1 \cdot T_{em}$ and $V_{gen} = k_2 \cdot \omega_{mech}$, where k_1 and k_2 are constants. Inserted in ohms law and applying passive loading, equation 2.4.2 is obtained:

$$R_{gen} = \frac{V_{gen}}{I_{gen}} = \frac{k_2 \cdot \omega_m}{k_1 T_{em}} = k_3 \frac{1}{B_{damp}} \tag{2.4.2}$$

$$B_{damp} = \frac{k_3}{R_{gen}} \tag{2.4.3}$$

Where R_{gen} is the equivalent load resistance. This is a simplified relation, but important to understand the connection between R and B.

The relation between R_{phase} in a star connected 3-phase load and R_{DC} in a circuit containing a diode rectifier is needed to be known. Why this is necessary becomes clear later. The starting point for finding the relation is equality of power in the two cases.

$$\begin{aligned} P_{DC} &= P_{3phase} \\ I_{DC} \cdot V_{DC} &= 3 \cdot I_{phase} V_{phase} \cos\phi \end{aligned}$$

$\cos\phi$ is equal to 1 with a purely resistive load. Inserting $I_{DC} = \frac{V_{DC}}{R_{DC}}$ and $I_{phase} = \frac{V_{phase}}{R_{phase}}$ we get:

$$\begin{aligned} \frac{V_{DC}^2}{R_{DC}} &= 3 \cdot \frac{V_{phase}^2}{R_{phase}} \\ \frac{V_{DC}^2}{R_{DC}} &= \frac{V_{LL}^2}{R_{phase}} \end{aligned}$$

Inserting the relation between V_{LL} and V_d in equation 2.1.2.

$$\frac{R_{phase}}{R_{DC}} = \frac{V_{LL}^2}{(1.35V_{LL} - \frac{\pi}{3}\omega L_s I_d)^2}$$

where ω is electric frequency in $\frac{rad}{s}$. A simplification is done; the losses in the generator is neglected and the open circuit induced voltage, E_a, become equal to V_{LL}. In generator mode is E_a bigger than V_{LL} at all times which have to be taken into account when evaluating the relation. By applying equation 2.2.4 and 2.2.6 ω can be substituted for an expression including V_{LL}:

$$\frac{R_{phase}}{R_{DC}} = \frac{V_{LL}^2}{(1.35V_{LL} - \frac{\pi}{30}\frac{p}{2}\frac{\sqrt{2}}{k_E}\frac{\pi}{3}L_s I_d \cdot V_{LL})^2}$$

$$\sqrt{\frac{R_{phase}}{R_{DC}}} = \sqrt{\frac{V_{LL}^2}{(1.35V_{LL} - \frac{\pi}{30}\frac{p}{2}\frac{\sqrt{2}}{k_E}\frac{\pi}{3}L_s I_d \cdot V_{LL})^2}}$$

$$\sqrt{\frac{R_{phase}}{R_{DC}}} = \frac{V_{LL}}{1.35V_{LL} - \frac{\pi}{30}\frac{p}{2}\frac{\sqrt{2}}{k_E}\frac{\pi}{3}L_s I_d \cdot V_{LL}}$$

By dividing with V_{LL} and squaring the relationship between R_{DC} and R_{phase} is obtained:

$$R_{DC} = (1.35 - \frac{\pi^2 p\sqrt{2}}{180k_E}L_s \cdot I_d)^2 R_{phase} \tag{2.4.4}$$

The negative term is smaller than expressed, because of the assumption made, but the error done should not be more than a few % depending on the generators parameters, L_g and R_g.

3 Laboratory setup and parameters

Note that generator force and generator torque is practically the same. For the FO-rig is the only difference the linear to angular gear ratio. The two terms are used back and forth.

3.1 System description and laboratory setup

The system investigated is given in figure 3.1.1.

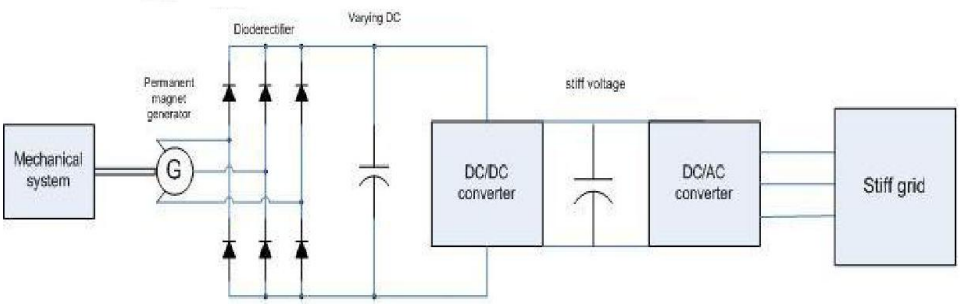

Figure 3.1.1: The converter setting that will be investegated in this work

At the left, the mechanical system representing the movement of the point absorber is presented. By a gear which converts linear motion to rotational motion the shaft speed is given. A permanent magnet rotational generator is used as power take off device. A PMG has the advantage of high pole number which is suitable for converting low speed waves into high frequency induced voltage. The generated current is rectified and put into a supposed small DC-link. The idea of the concept is to control DC-link voltage with a DC/DC converter to indirectly control the generated current and thus the electromagnetic torque. At a given generator speed, a high DC-link voltage will give a low current and vice versa. This work will not focus on grid interfaces and the voltage at the grid side is assumed stiff independent of input power from the WEC.

The converter setting in figure 3.1.1 is observed in wind power simulations [9][10]. The DC-link voltage is then designed to have a close to constant value because of the nearly constant power from the wind. This differs from a direct drive wave energy converter of same design because power fluctuates between zero and maximum during one cycle and the DC-link voltage will have to be regulated constantly because of this. For a commercial wave energy power plant of this kind, several WEC's will be connected together with at a stiff voltage and have a common DC/AC inverter. The fluctuations in power output will be then be reduced[3]. Stiff voltage can therefore be selected at a desirable level in the simulations since only one WEC is looked at.

In order to implement the system in a laboratory setup is two electrical machines on a mutual shaft used, an induction motor and a PMG. The induction motor represents the mechanical system in figure 3.1.1and is oversized in order to give the desired speed input to the generator, independent of the torque applied by it. The PMG used was a Gin Long PMG 1800, star connected. It had 16 poles and 3.9 ampere of rated current, for additional information see appendix B. The reason for testing this exact generator was because it is the same as used at the FO-rig. The electrical machine set up is shown in figure 3.1.2.

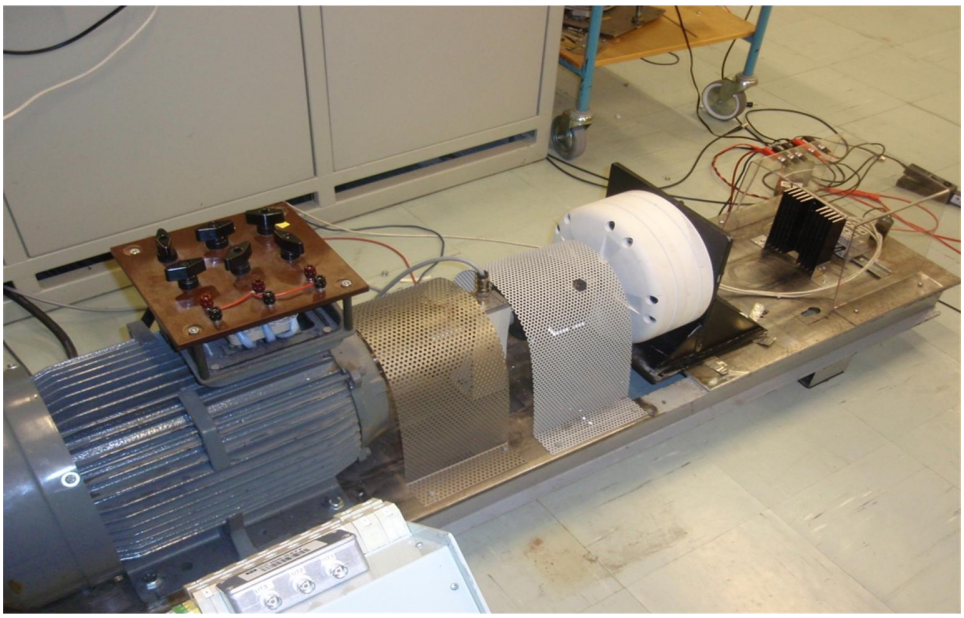

Figure 3.1.2: Laboratory setup with induction motor(left) and Permanent magnet generator(right).

The DC-DC converter in figure 3.1.1 is in the lab set up represented by different resistors depending on the desired damping constant of the converter. This is a good representation of an ideally working converter with passive loading control as discussed in chapter 2.4. The rest of the system is not implemented in the laboratory setup i.e. the stiff DC voltage and grid interface.

The laboratory setup is shown in figure 3.1.3.

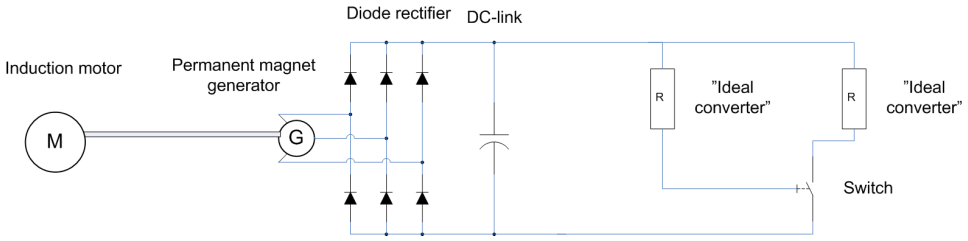

Figure 3.1.3: Lab setup representing the system.

The switch and the second resistor are only used for transient tests. For steady state tests and tests with dynamic input only one resistor without the switch is used.

The induction motor has a regular back to back frequency converter connected to be able to apply the desired shaft speed. An analogue 10 volts input was used to give the speed reference. The frequency converter had problems with supplying frequencies below 2 Hz which corresponds to a shaft speed of 60 RPM for a for four pole machine. If a reference voltage corresponding to a lower frequency than 2 Hz were applied, it caused the converter and thus the motor to stop. This was not ideal since it was desirable to control the shaft speed from 0 to 450 rpm in order to get authentic wave input to the generator. Speeds of less than 60 rpm cannot be observed in the laboratory results because of this. The problem with the frequency converter did not cause any problems apart from not getting the desired input, laboratory tests could still be compared with simulations. For tests with dynamic input a signal generator with a sinusoidal voltage was used to give the frequency converters speed reference. The period and amplitude of the signal was adjusted to control the wave period, T_s, and amplitude of the shaft speed. A DC-offset was added to the signal to avoid the motor from stopping.

The control desk, diode rectifier and DC-link is shown in figure 3.1.4.

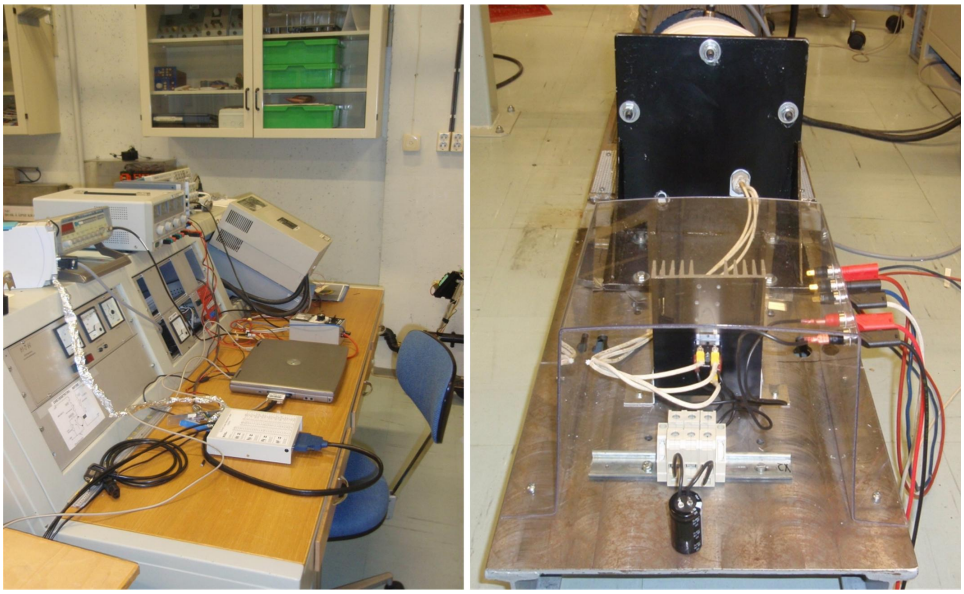

Figure 3.1.4: Left: Control station with frequency converter and PC with Labview interface. Right: Diode rectifier and DC-link capacitor.

3.2 Measurements and Scaling

Scaling measurements is an important task in order to verify simulation models. If measurements are scaled wrong, it will seem like simulations are wrong even though they might be good. A Labview interface was used for logging when varying input speed was applied. Four different variables were logged and thus needed to be scaled.

The measurement set up used for scaling operation is shown in figure 3.2.1 and variables needed to be scaled and the measurement equipment used are given in table 3.2.1.

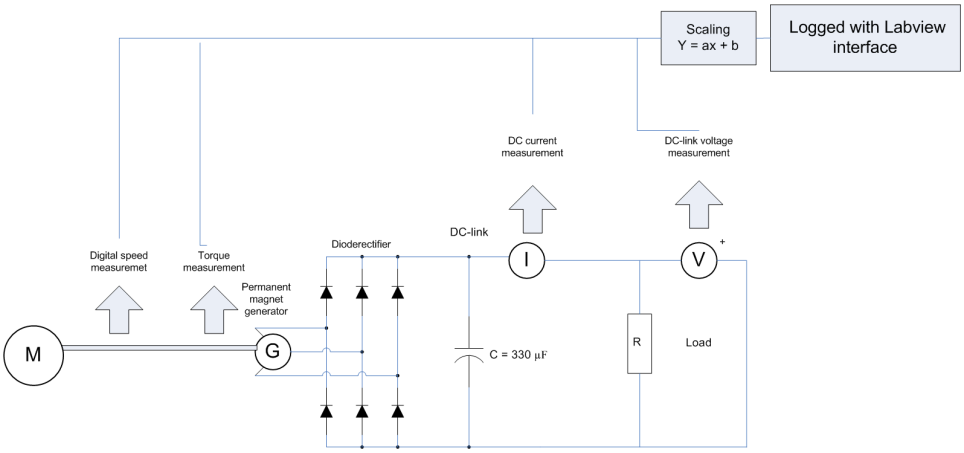

Figure 3.2.1: Lab setup for measuring and scaling

Variable	**Measuring device, Reg.nr**	**Logging device, Reg.nr**
Current	Fluke 112 multimeter, S03-0353	Trafoshunt LA 50-P,I04-191
Voltage	Fluke 112 multimeter,S03-0357	LEM Voltage module LV 100,I05-0011
Torque	HBM MP 55,N04-0060	HBM torque transducer T5,065130061
Speed	Line Seiki TM 4010,N06 0073	Heidenhain ERN 420,2048 28S12-31

Table 3.2.1: Equipment used for measuring, logging and scaling

Three different steady state speeds with two different loads, R, were measured with the specified measurement equipment and logged with the Labview interface. The mean values of the logged signals where then compared and scaled with the measured once. After logged signals were scaled, new measurements were done and compared with the logged values to verify that the scaling had sufficient accuracy. All scaling proved to be good except for the current scaling, which had over 5 % deviation compared to measured values. The output signal from the current measurement device showed to be too small and hence vulnerable to disturbances. To solve the problem 10 turns were applied in the current measurement loop instead of the single turn first used. The modification resulted in a accurate current logging with less than 0.2 % deviation.

The scaling results are presented in table 3.2.

Measured	Logged	Dev %	Measured	Logged	Dev %
Voltage	$R = 80ohm$		**Current**	$R = 80ohm$	
83	82.95	0.06	2.104	2.101	0.13
142.3	142.4	-0.07	2.532	2.532	0.09
208	208.14	-0.07	2.911	2.911	-0.01
Voltage	$R = 28ohm$		**Current**	$R = 28ohm$	
38.8	38.92	-0.32	1.333	1.332	0.10
77.40	77.38	0.02	2.697	2.701	-0.15
130.5	130.69	-0.14	4.609	4.604	0.11
Torque	$R = 80ohm$		**Speed**	$R = 80ohm$	
8.75	8.73	0.23	113.5	112.97	0.47
14.50	14.53	-0.18	194.6	193.36	0.64
20.75	20.76	-0,03	286.7	284.21	0.87
Torque	$R = 28ohm$		**Speed**	$R = 28ohm$	
11.5	11.49	0.06	64.3	64.80	-0.77
22.15	22.17	-0.07	127.30	127.97	-0.53
36.30	36.26	0.11	219.40	219.29	0.05

Table 3.2.2: Deviations between measured and logged parameters after scaling.

The deviations of the measurements are all under 1% which is acceptable precession, since the DC-accuracy of the multimeter used is ±1.0% [11]. The most uncertain measurement is logged speed.

3.3 Estimation of generator parameters

Table 3.3.1 show the generator parameters estimated in this section. The process was more time consuming and cumbersome than excepted.

Parameter	Value
Voltage constant k_E	0.885 $\frac{VLL_{peak}}{RPM}$
Generator internal resistance R_g	4.9 ohm
Generator internal inductance L_g	23.9 mH

Table 3.3.1: Generator parameters at $20°C$

The PMG used was poorly documented and it was thus necessary to estimate the generator parameters exactly by measurements. The task seemed straight forward and easily manageable. But things did not turn out that way. A lot of effort and time was used to this assignment and early measurements indicated that the generator inductance was inverse proportional

to the shaft speed, which seemed quite unrealistic. There was no access to the star point of the generator, which made the task harder. If there had been access to the star point could the generator inductance easily be measured with a RLC-meter. But using a RLC-meter without access would require measurement over two phases and give wrong result due to mutual inductance between the phases measured.

The generators voltage constant, k_E, was estimated by measuring the line to line voltage of the generator at open circuit. Different speeds from 60 to 450 rpm were used. Five series were done in total to reduce uncertainty in the measurements. The results are shown in figure 3.3.1.

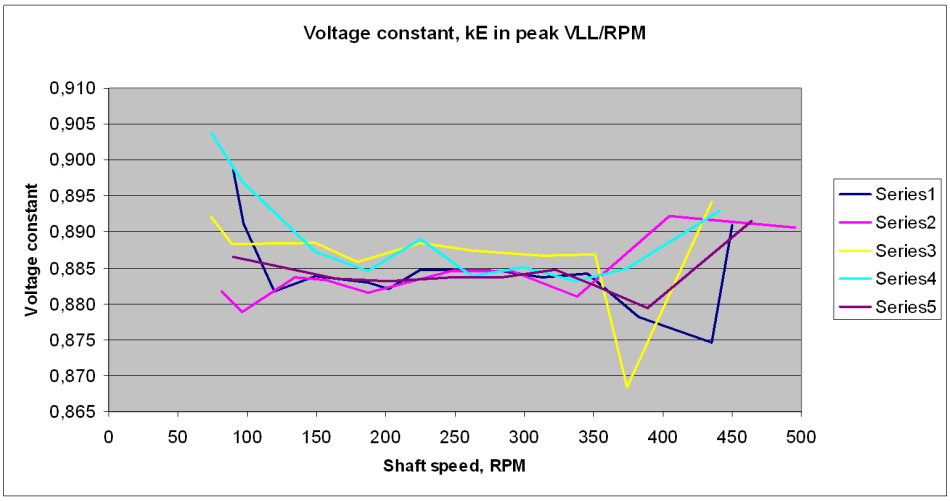

Figure 3.3.1: Voltage constant as function of shaft speed

By taking the average of all the measurements was the voltage constant estimated to $0.885\frac{VLL_{peak}}{RPM}$. This is 6.2 % higher than the documentation given for the generator, appendix B.

The internal resistance of the generator was measured by applying a DC-current over two phases, generator inductance can then be neglected. The voltage was measured and the resistance could be calculated. Phase inductance was obtained by dividing the measurement result by two. The measurement method is more accurate than a ohmic measurement on a multimeter, espessially at low resistances [11].

By knowing both the internal resistance of the generator and the voltage constant the generator inductance could be calculated by measurements. The measurement setup is shown in figure 3.3.2.

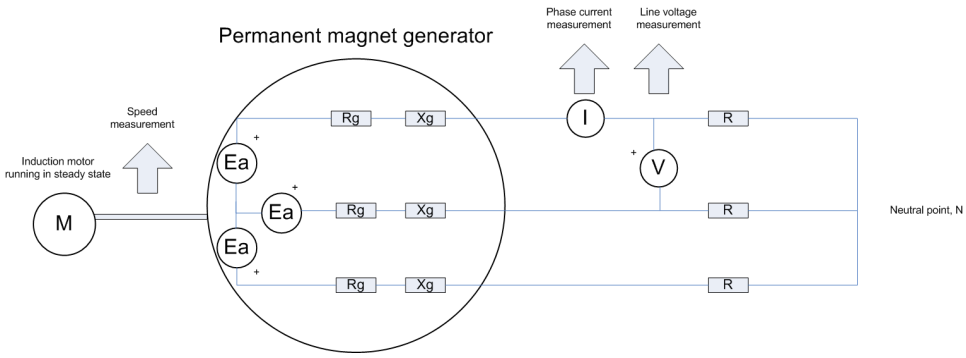

Figure 3.3.2: Circuit diagram for inductance measurements.

Speed measurement was used to calculate the internal induced voltage, Ea, based on the voltage constant previously estimated. The resistance of the generator, R_g, and load, R, were known and the only unknown parameter was X. Generator phase inductance could be calculated by dividing by the electrical frequency as shown in equation 3.3.1.

$$L_g = \frac{X}{\omega_{electric}} = \frac{\sqrt{Z^2 - R^2}}{\frac{p}{2}\omega_{mech}} = \frac{\sqrt{(\frac{\omega_{mech} k_E}{I_{phRMS}\sqrt{3}})^2 - (\frac{V_{LL-RMS}}{I_{phRMS}\sqrt{3}} + R_g)^2}}{\frac{p}{2}\omega_{mech}} \quad (3.3.1)$$

Measurements were done for ω_{mech} from 60 to 450 rpm with different loads, R, and calculations of the inductance were done for every sample. R is calculated by V_{LL-RMS} and I_{phRMS} instead of being measured with a multimeter because of higher precision. Tests indicated a varying inductance with speeds. The results were quite unrealistic since the generator inductance was measured to be 3 times higher at low speeds. New tests were preformed at constant speed with different loads. With these tests was current the only varying parameter, and it could be examined if the strange test results were caused by saturation phenomena in the machine. The chosen speed was 300 rpm, which is in the middle of the generators area of operation. Strangely enough was the same phenomena observed in 4 out of 5 series. At low current was the inductance high and vice versa, even though the generator current was below rated. In the first test was R bigger than Z and L_g could not be calculated and was set to zero.

The measurement data are presented in figure 3.3.3.

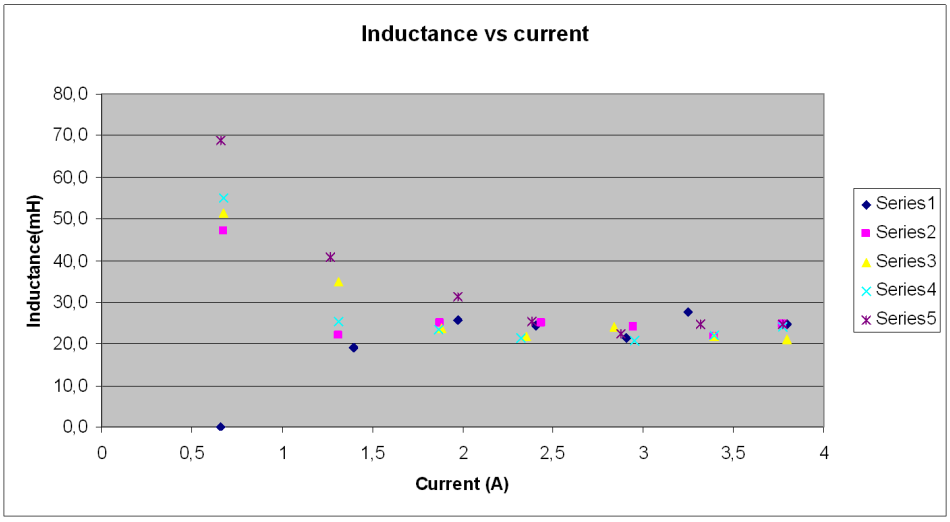

Figure 3.3.3: Inductance as function of current

The series are in chronological order so series 1 was the first and series 5 the last to be recorded. The tendency is a clearly rising inductance at low currents. This could indicate some kind of temperature dependency. The sensitivity of the previous estimated voltage constant were tested by changing the assumed constant a small step of 1% and perform the same calculation. The results were surprising. $\pm 1\%$ change of k_E resulted in inductances ranging from 0 to 116 mH for small currents, which indicated extreme sensitivity. For higher currents was the change of results not that extreme.

The sensitivity is given in figure 3.3.4.

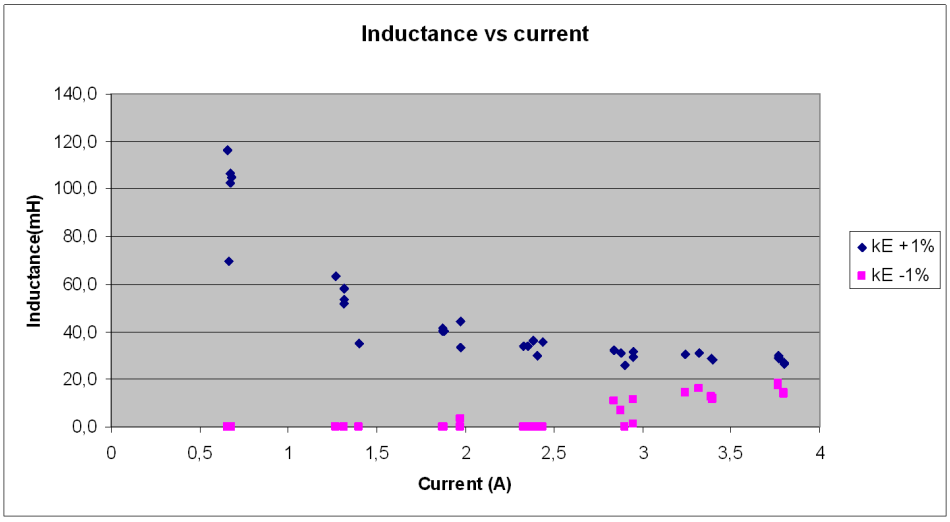

Figure 3.3.4: Inductance calcultaion with 1 % change of kE. kE = 0.876 and kE = 0.894

These results indicated that inductance measurements at low currents were useless if the voltage constant was temperature dependent. A new open circuit voltage test after the generator had been working for a while was done. The machine worked at its rated speed and current for five minutes and an open circuit test was performed. The same procedure with five test series was used. The results are shown in figure 3.3.5

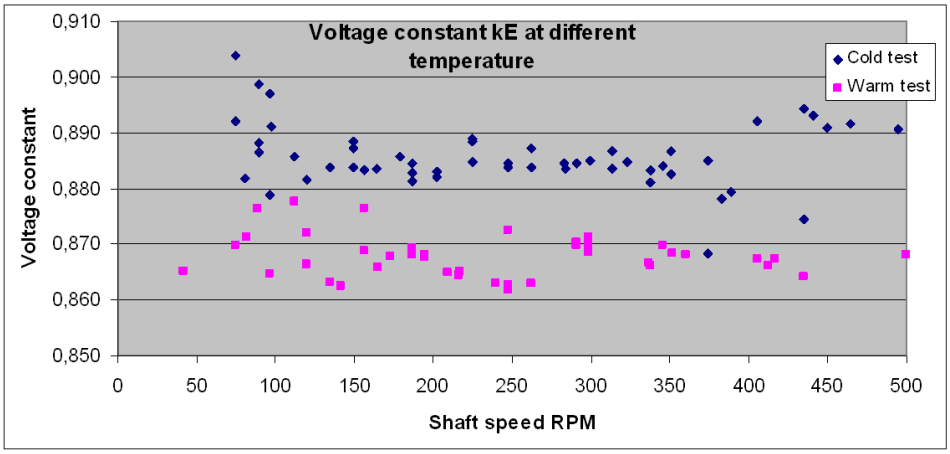

Figure 3.3.5: Voltage constant before and after the generator have been working

The difference between the two tests series was significant. Mean voltage constant of the warm test series was 0.868 that is 1.9% lower than the cold series. This implies that inductance measurements at low currents had considerable uncertainty. By looking at figure 3.3.4, it also implies that inductance tests at high currents are most robust and should be used for calculation of L_g. The inductance was calculated to 23.9 mH by using the five initial test with largest current. The reason for the decreased voltage constant was temperature dependency of the rotor magnets. The magnets are a NdFeB(Neodymium Iron Boron) type with relatively high maximum energy product i.e. good energy density. The drawback of these magnets is low Curie temperature which implies a large temperature coefficient. They loose relatively much magnetization per $^{\circ}C$ increase [12] [13].
The temperature dependency was also tested for the generator resistance, R_g. A similar test as earlier described was done after the generator had been working. The test indicated 5.2 ohm per phase, which is 6% more than the cold test result. The increased resistance made it look like a decrease in the inductance, as can be seen in equation 3.3.1. However the contribution could be neglected compared to the effects of the decreasing voltage constant.

3.4 Selecting resistor values

A converter with passive loading control can be modelled as a resistor, as shown in chapter 2.4. The relationship between R and B depends on the mechanical and electrical properties of the individual system. The relation between R and B has already been identified for the FO-rig. The major difference between the lab experiments in this work and the FO-rig is that the generator at the rig had a star connected three phase load and for the lab experiments a DC-load will be used. The relation between a 3-pahse load and a DC-load is thus needed to be known in order to apply the desired damping constant in the lab.

A curve based on four measurement from the FO-rig is presented in figure 3.4.1

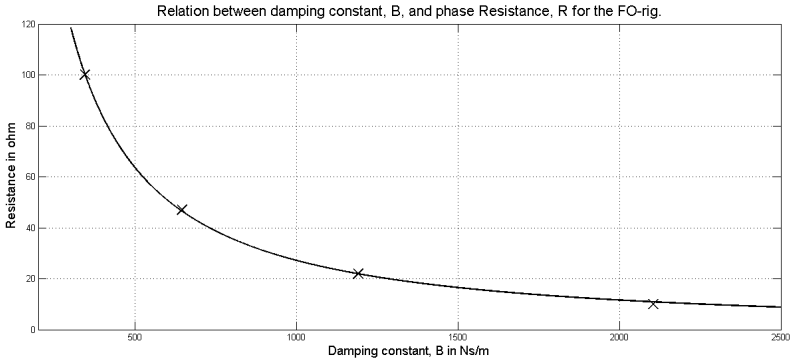

Figure 3.4.1: Relation between B_{damp} and R_{phase}, the crosses are test results from the FO-rig.

The curve is made by plotting the four measurement points into a program called "curve expert 1.3". By a power regression the four points were adjusted to the best fitting curve. The curve equation is presented in equation 3.4.1

$$R_{phase} = 1.3 \cdot 10^5 \cdot {B_{damp}}^{-1.21} \tag{3.4.1}$$

It can be observed that the relation is fairly close to the result of the simplified analogy in equation 2.4.2. In the project work was a damping constant of 700 and 1200 $\frac{Ns}{m}$ used because they were calculated to be in the optimal range for maximizing power output from the WEC. For the laboratory tests in this work a wider range of damping constants have been used to get a broad range of data for the system. The selected damping values are between 500 and 1500 $\frac{Ns}{m}$. With a DC-current current of 2.4 ampere, which corresponds to half of rated generator current, equation 2.1.5, and applying equation 3.4.1 and 2.4.4, the relation between DC resistance corresponding to the selected damping values can be calculated:

$$R_{DC-500} = 1.3 \cdot 10^5 \cdot 500^{-1.21} \cdot (1.35 - 0.067)^2 \approx 120 ohms \tag{3.4.2}$$

$$R_{DC-1500} = 1.3 \cdot 10^5 \cdot 1500^{-1.21} \cdot (1,35 - 0.067)^2 \approx 30 ohms \tag{3.4.3}$$

30 and 120 ohms set the boundaries for operation of the system since these values correspond to the desired damping values. Throughout this work four resistance values will be used for representing different damping constants of the converter; 30, 50, 80 and 120 ohms. This covers the necessary span of operation for the generator and the system.

4 Experimental results and linearization

Three types of experiments have been done. A steady state test, a test with dynamic input speed and a transient analysis.

4.1 Steady state analysis

The test setup was in accordance with figure 3.1.3 and the simulation model is given in figure 4.1.1.

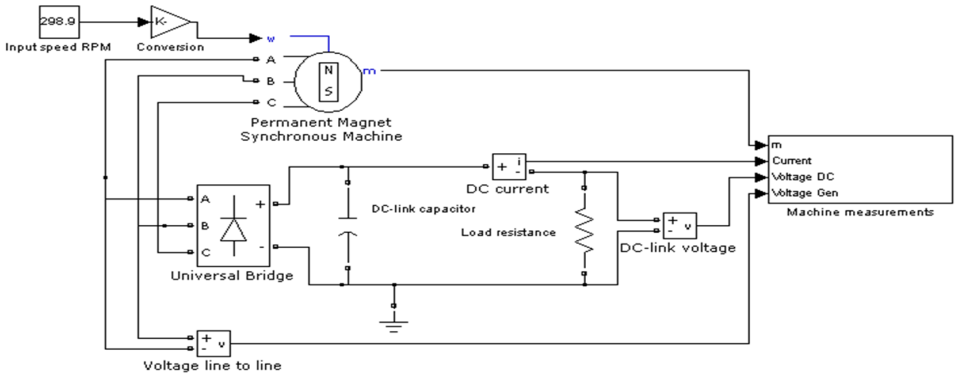

Figure 4.1.1: Simulink model for steady state simulation analysis

Constant shaft speeds were applied and the DC-current, DC-link voltage and torque were then measured. Seven speeds, evenly distributed over the rated range of the generator, were applied for each of the four resistor values. For the 30 ohm test no higher speeds than 290 RPM were applied since the current became as high as 6 ampere. Measurement devices used are the same as in table 3.2.1. The DC-link capacitor was 330 μF as calculated in the project work. For the simulations the same speed as measured in the lab tests were applied.

The results from the measurements, simulations and comparisons are shown in table 4.1.1

Speed RPM	**DC Voltage** meas , sim	**diff** ±%	**DC current** meas, sim	**diff** ±%	**Torque** meas, sim	**diff** ±%
Load resistance 120 ohm						
78.2	59.0 , 59.1	-0.2	0.49 , 0.49	0.0	4.6 , 4,0	13.0
122.7	93.2 , 92.9	0.3	0.78 , 0.78	0.0	6.9 , 6.2	10.1
181.0	137.2 , 136.7	0.4	1.14 , 1.14	0.0	9.8 , 9.0	8.2
239.9	181.2 , 180,2	0.6	1.51 , 1.50	0.7	12.7 , 11.8	7.1
303.6	228.8 , 226.4	1.0	1.91 , 1,89	1.1	15.8 , 14.7	7.0
378.1	283.2 , 279.5	1.3	2.36 , 2.33	1.3	19.3 , 17.9	7.3
449.7	334.7 , 329.7	1.5	2.80 , 2.76	1.4	22.6 , 21.0	7.1
Load resistance 80 ohm						
70.9	51.5 , 51.4	0.2	0.67 , 0.67	0.0	5.5 , 5.3	3.6
148.3	108.6 , 108,3	0.3	1.41 , 1.41	0.0	11.2 , 11	1.8
192.2	140.3 , 139.9	0.3	1.83 , 1.83	0.0	14.2 , 14.2	0
257.1	186.5 , 186.0	0.3	2.43 , 2.42	0.4	18,6 , 18.7	-0.5
321.0	231.5 , 230.6	0.4	3.03 , 3.02	0.3	22.9 , 23.1	-0.9
359.1	257.7 , 256.6	0.5	3.38 , 3.37	0.3	25.2 , 25.6	-1.6
501.3	358.0 , 351.1	1.8	4.70 , 4.61	1.9	34.3 , 34.3	0.0
Load resistance 50 ohm						
68.6	46.0 , 46,2	-0.4	1.00 , 1.00	0.0	8.5 , 7.9	7.1
112.4	76.0 , 75.5	0.7	1.70 , 1.69	0.6	13.7 , 13.2	3.6
188.7	126.7 , 125,9	0.6	1.80 , 2.78	0.7	22.3 , 21.4	4.0
250.0	166.0 , 165,2	0.5	3.63 , 3.61	0.6	28.7 , 27.4	4.5
288.2	189.5 , 180.0	0.3	4.10 , 4.09	0.2	32.5 , 30.7	5.5
361.1	234.0 , 233.2	0.3	5.10 , 5.08	0.4	39.5 , 37.4	5.3
445.2	281.9 , 282.0	0.0	6.20 , 6.20	0.0	46.5 , 44.7	3.9
Load resistance 30 ohm						
64.2	38.5 , 38.7	-0.5	1.37 , 1.38	-0.7	11.4 , 10.9	4.4
108.2	65.0 , 65.4	-0.6	2.31 , 2.33	-0.9	18.7 , 18.1	3.2
133.9	80.3 , 80.7	-0.5	2.85 , 2.86	-0.4	22.9 , 22.1	3.5
170.0	101.0 , 101.6	-0.6	3.59 , 3.61	-0.5	28.4 , 27.4	3.5
223.0	130.8 , 131.1	-0.4	4.67 , 4.69	-0.5	36.2 , 34.8	3.9
249.2	144.7 , 145.3	-0.4	5.18 , 5.19	-0.3	39.8 , 38.2	4.0
290.4	166.3 , 167.3	-0.6	5.97 , 6.00	-0.5	45.3 , 43.5	4.0

Table 4.1.1: Steady state measurments and simulations at the four working points

The current and voltage measurements concur well with the simulated values. Most of the deviations are under 1% and the maximum deviation is 1.9% which is acceptable when considering possible sources of error; the DC-link capacitor, the diode rectifier and the measurement devices. The multimeter used has a DC-accuracy of $\pm 1.0\%$ which imply that the results from the steady state analysis are very good. When considering measured and simulated torque are the deviations bigger. This is actually fairly plausible. Except for some tests with 80 ohms is simulated torque lower than the measured torque. A likely reason for this is that measured torque is mechanical shaft torque and simulated torque is electromechanical. The simulation do not account for start up torque, friction and windage losses. For all the test series is the deviation biggest at low speeds. This indicates that the start up torque is quite significant for low torque values. The deviations decline for the next speed input, making the start up torque less significant. For the 30 and 50 ohm series does the torque deviation have a slight increase with speed which can indicate a speed dependent friction torque. However is the tendency not observed with 80 and 120 ohms and therefore not a significant trend. Patterns of windage losses, which is proportional to the speed squared, cannot be observed from the tests, this is likely because the tests are done at relatively low speeds. The deviations are biggest for the 120 ohms series.

4.2 Dynamic input analysis

Tests with dynamic speed input was done in accordance with figure 3.2.1. For simulations, the same model was used as for steady state analysis. The only difference was that speed input to the model was the time varying speed logged in the laboratory tests. The four resistors representing damping constants of the converter were used during testing with two different wave periods, Ts, in all eight test series. One with Ts approximately two seconds and one with approximately four seconds. Waves with two seconds period is typical for the wave climate at the FO-rig as can be seen in appendix **??**. The four seconds wave was selected to get a broader data range. The torque measurement device, HBM MP 55, filters the torque before it is logged.

An example of torque measurement and simulation are presented in figure 4.2.1.

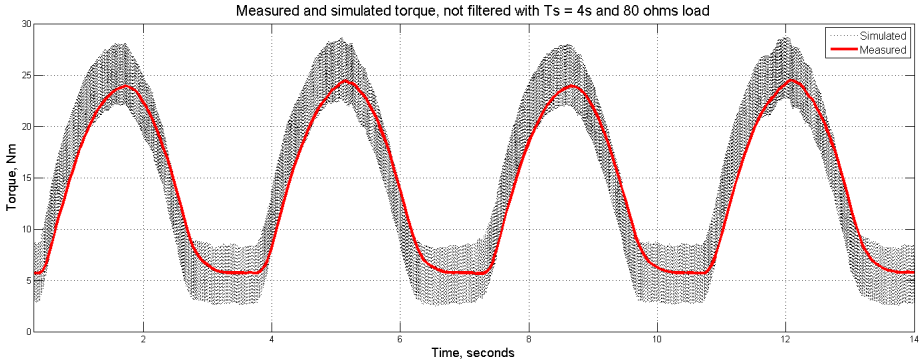

Figure 4.2.1: Measured and simulated torque without filter on the simulation.

The simulated torque includes torque ripple. It is difficult to get any information from such results and a filter is applied to the simulated results to be able to compare the two curves. The filter used on the measured torque is an advanced Bessel filter averaging over one second [14]. A moving average filter was applied on the simulation results in order to be able to compare the results. The averaging period of the filter were experimentally tuned to fit the time delay of the measured signal. An averaging period of 1143 data points proved to be a good approximation of the Bessel filter in the HBM MP 55 module. The result after the filtering process is presented in figure 4.2.2.

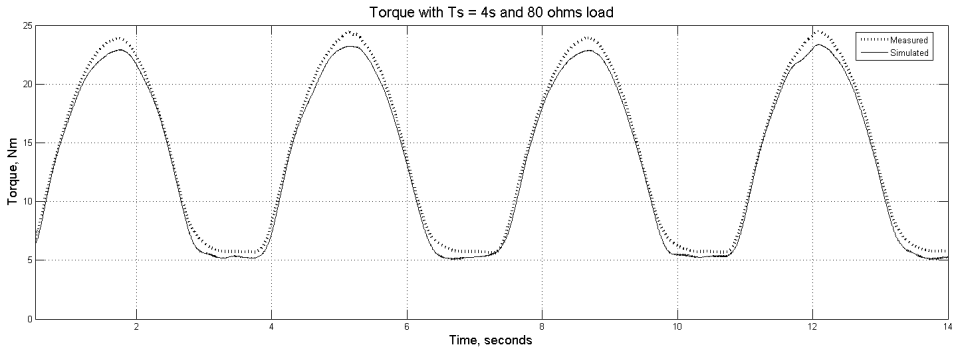

Figure 4.2.2: Measured and simulated torque with moving average filter on the simulation.

The same moving average filter is applied on all the simulated torque tests.

Results for current and voltage test with 80 ohms load and Ts = 4s is presented in figure 4.2.3 and 4.2.4.

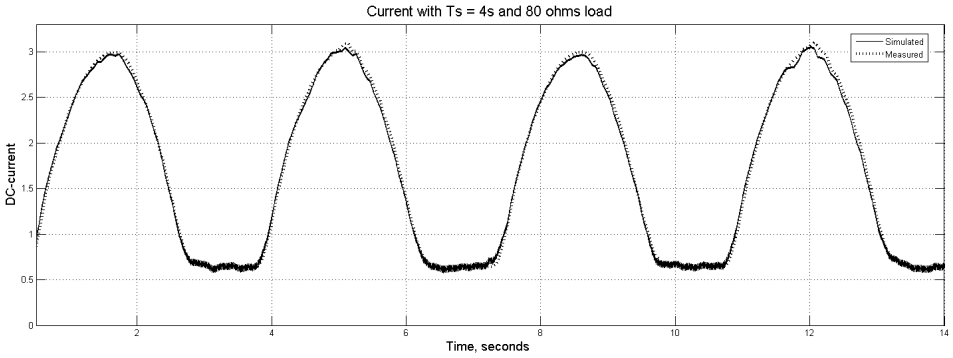

Figure 4.2.3: Measured and simulated current 80 ohms and four second wave period.

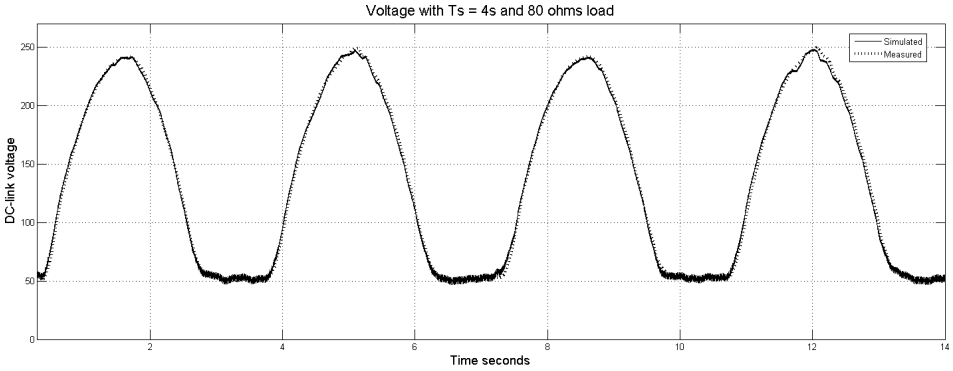

Figure 4.2.4: Measured and simulated voltage 80 ohms and four second wave period .

Measured and simulated results for 120 ohms load and Ts = 2s are given in figures 4.2.5-4.2.7

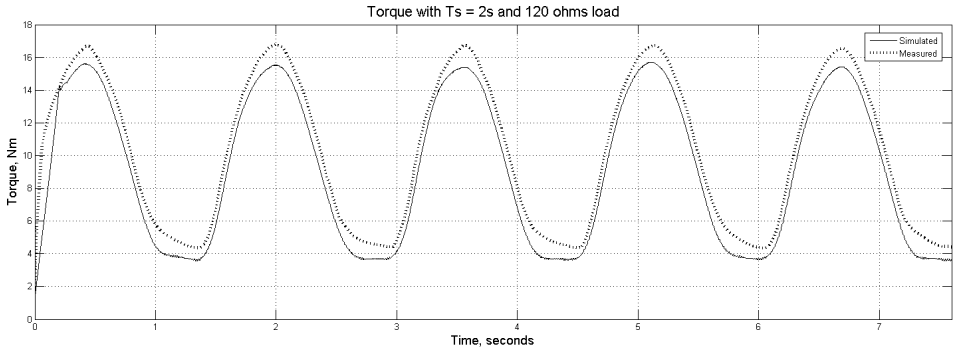

Figure 4.2.5: Measured and simulated torque, 120 ohms and two second wave period .

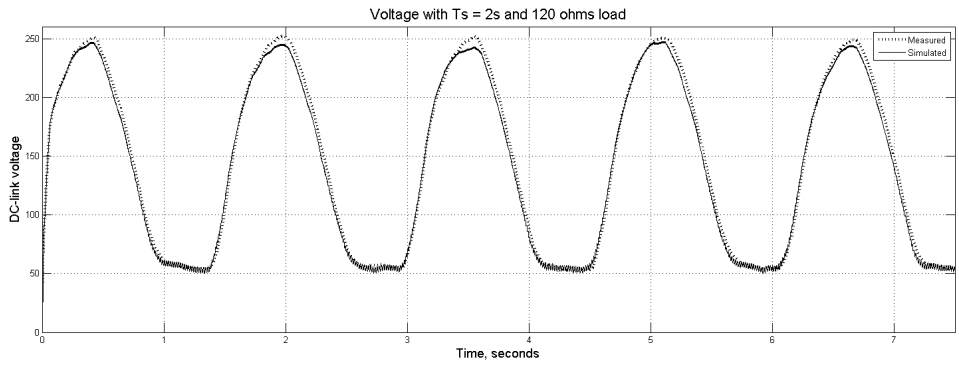

Figure 4.2.6: Measured and simulated voltage, 120 ohms and two seconds wave period .

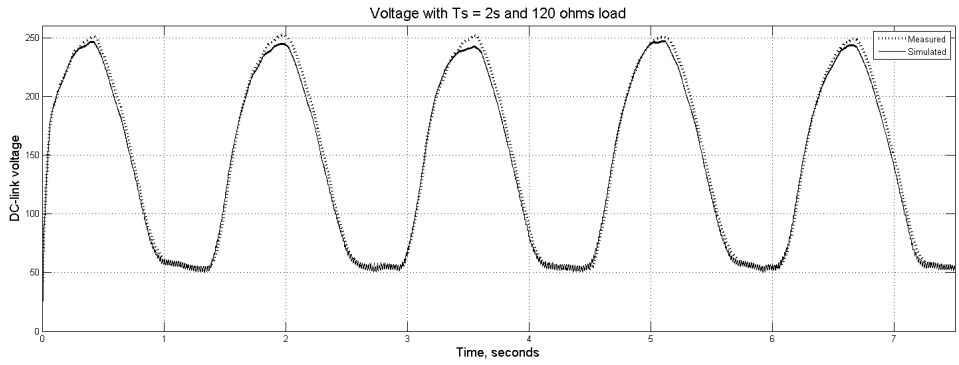

Figure 4.2.7: Measured and simulated current 120 ohms and two seconds wave period.

The simulated current have practically no ripple compared to the torque. This is because its measurement point, figure 3.2.1, is on the far side of the DC-link. It is reasonable to assume that the generator current on the generator side of the DC-link has the same proportion of ripple as the torque, since they are proportional. A small ripple can be observed both for the

simulated DC-link voltage and the DC-current. This cannot be observed on the measured curves, this is because the logging frequency was 50 Hz which is to low for capture the ripple. The measurements were not so smooth because of this, and a rough version of the moving average filter used for the toque simulations was applied. The averaging period was selected to five data points to get a smoothing effect without a noticeable time delay. The results from the dynamic input analysis are good and the simulated

and measured results concur well. The simulated torque is smaller than the measured for all the tests except for one of the 50 ohm series. This coincides with the steady state analysis and the same argumentation for explaining the deviations is applicable. The maximum deviations in amplitude occur at peaks. To systematize the peak deviations they have been summarized in table 4.2.1. The deviation percentages for the torque tests are bigger at low torque, this is probably because of the earlier mentioned start up torque. Figures of the remaining tests can be found in appendix A.

	Voltage dev %	**Current dev** %	**Torque dev** %
120 ohms			
Ts = 4s	2.8	3.4	8.7
Ts = 2s	4.0	4.8	7.8
80 ohms			
Ts = 4s	0.8	1.6	4.9
Ts = 2s	2.8	3.1	4.5
50 ohms			
Ts = 4s	-0.9	1.6	-2.3
Ts = 2s	-2.1	-2.5	1.7
30 ohms			
Ts = 4s	3.0	2.7	5.5
Ts = 2s	2.3	3.0	2.4

Table 4.2.1: Deviations at wave peaks between measured and simulated results for dynamic input analysis.

4.3 Transient analysis

4.3.1 Transient measurements and simulation

Verifying transient simulations is important in order to obtain a dynamic model of the system. And on the basis of this be able making a linearized model of the system. Steps between two of the working points have been done and the transient response was logged with an oscilloscope. The step between two working states represents a step in the converters damping constant reference, B_{damp}, as earlier mentioned. Two different DC-link capacitors were used to get different responses. One with $330\mu F$ capacitance as previous used and one with 68 μF capacitance. The 68 μF DC-link capacitance was found experimentally by using the simulation model from the project work. In that model excitation force from waves was the input. A two times bigger wave than dimensioned were used as input and the DC-link capacitance was decreased until the system had stability problems. It occurred at approximately 68 μF. The simulation model used for transient simulations is presented in figure 4.3.1.

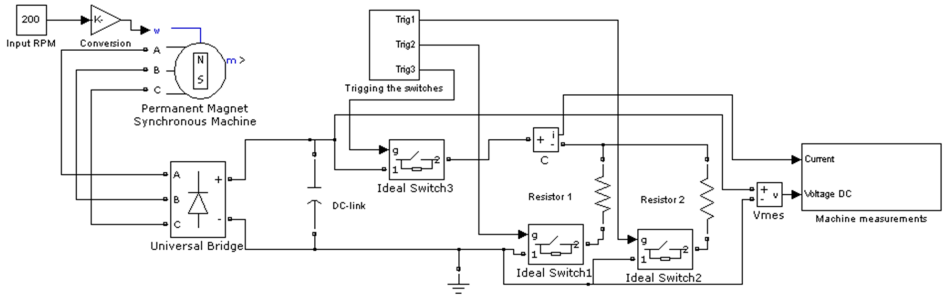

Figure 4.3.1: SIMULINK model used for transient simulations

It is the electrical transients that are interesting to investigate and not the mechanical. This to se how fast such a system can respond to a step in reference. The mechanical transient is not of any interest since it depends on factors such as how fast the frequency converter is and system inertia. These are factors which differ from the FO-rig. It was assumed that the total inertia of the system was sufficiently large to keep the speed constant during the electrical transient [15]. This is a reasonable assumption if no significant deviations change between simulated and measured voltage are observed during the electrical transients.

The results of the step responses are presented in figure 4.3.2 - 4.3.5:

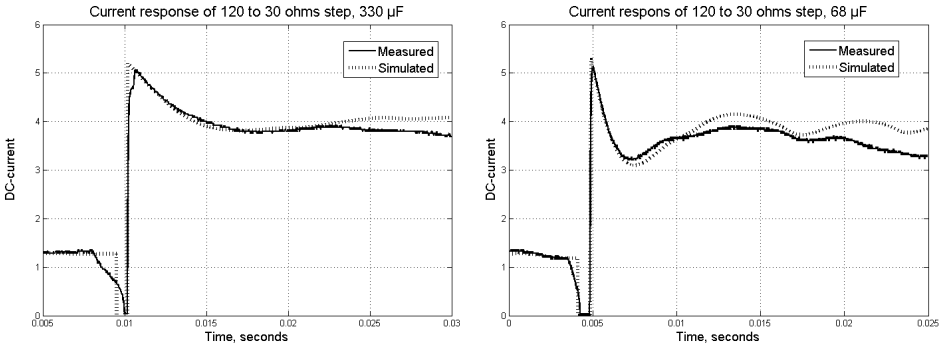

Figure 4.3.2: Current respons of step from 120 to 30 ohms at 200 rpm.

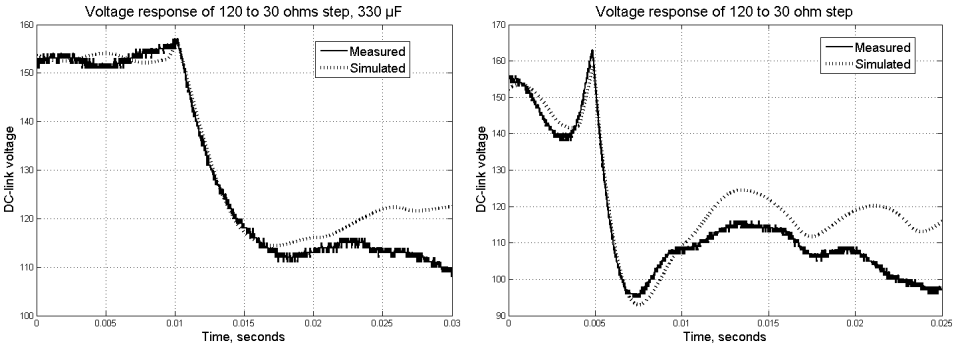

Figure 4.3.3: Voltage respons of step from 120 to 30 ohms at 200 rpm.

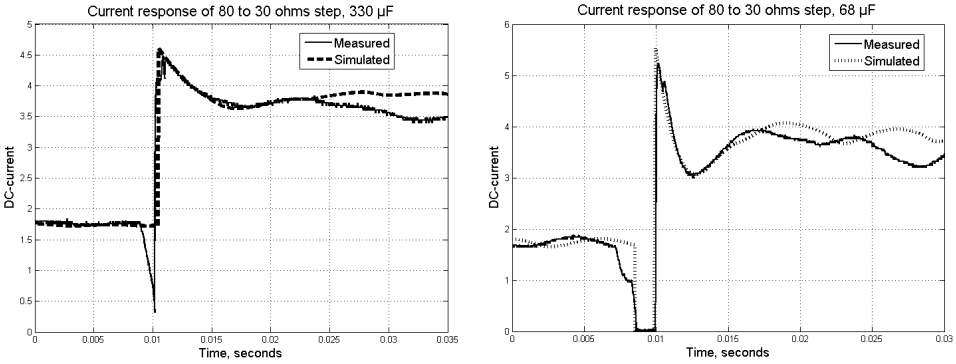

Figure 4.3.4: Current respons of step from 80 to 30 ohms at 190 rpm.

The step between two operating points was preformed with a mechanical switch. This was not ideal since the switch needed some time to change between the two states. This can be observed for 68 μF DC-link capacitance.

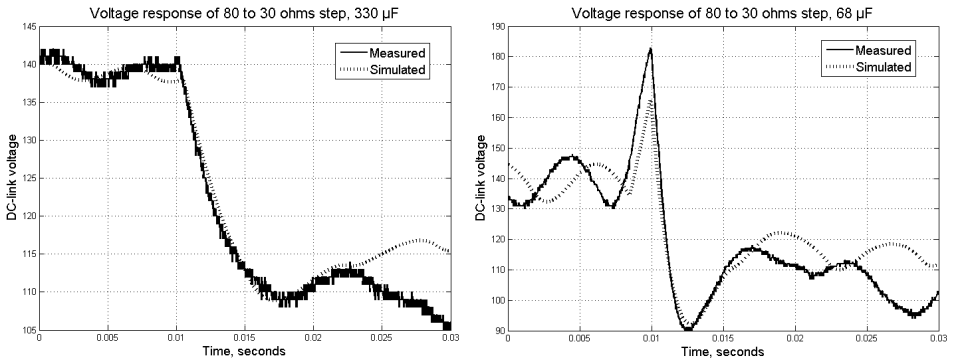

Figure 4.3.5: Voltage respons of step from 80 to 30 ohms at 190 rpm.

The switch was open for 1-2 ms and the generator current which cannot be turned off instantly because of generator inductance then was forced to enter the DC-link and thus increase DC-link voltage. The phenomena will be addressed as voltage build up henceforth. For the 330 μF capacitor tests does the voltage not build up, both because of shorter switching time and higher capacitance. Voltage build up would had been avoided if a semiconductor switch was used, commutation between the states had then been virtually instant. In order to coop with the phenomena was a third switch included in the simulation model in order to emulate the behaviour of the mechanical switch. The simulations and measurements concur well for approximately 15 ms after the step. The current and voltage then drops below the simulated values. This is likely because the simulations are done with constant speed independent of load torque but for the lab tests the increased load torque, due to higher damping, will decelerate the speed of the shaft. The response of the 68 μF tests are, not surprisingly, faster. By comparing the instant of the second peak value between the two capacitors can it be observed that the response of the 68 μF tests are roughly twice as fast.

4.3.2 Linearization

The main motivation for making a linearization is developing a general model to identify the time delay in the PTO of a WEC. This can be explained by the block diagram of a WEC in figure 4.3.1.

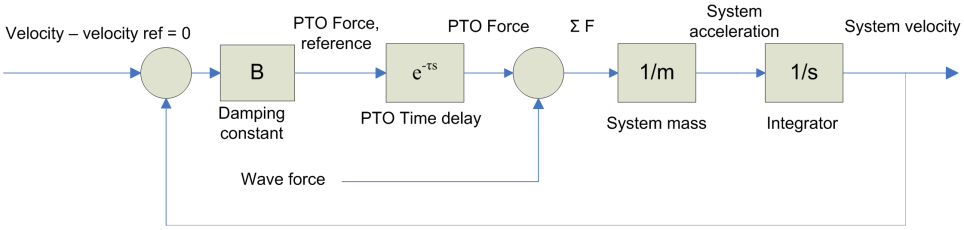

Figure 4.3.1: Block diagram of a WEC system.

The PTO represents here the generator and converter. These do not have instant response and thus represent a time delay. For the selected control, passive loading, it is desirable that PTO force and wave force act in opposite direction at all times. If the time delay in the PTO is too big, this will cause the forces to act in the same direction and lead to instability of the system.

The key parameters in the investegated system was identefied and a linearization based on the transient analysis was tried out and a fairly good approximation is presented in figure 4.3.2. For background material on control theory and Laplace transformation see [18] [19].

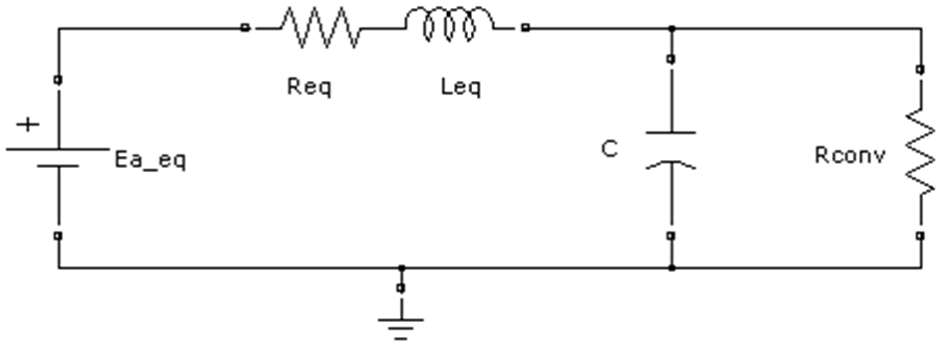

Figure 4.3.2: Linearization of the system.

Generator induced voltage, inductance and resistance are transformed to DC quantities by applying the necessary equations; 2.1.2 2.1.4, 2.1.3.

$$L_{eq} = 2 \cdot L_g = 47.8mH \tag{4.3.1}$$

$$R_{eq} = 2 \cdot R_g = 9.8ohm \tag{4.3.2}$$

$$E_{a-eq} = \frac{1.35k_E}{\sqrt{2}} \cdot \omega_m - \frac{3}{\pi} L_g \bar{I_d} \frac{p}{2} \frac{\pi}{30} \cdot \omega_m = \frac{1.35k_E}{\sqrt{2}} \cdot \omega_m - \frac{p}{20} L_g \bar{I_d} \cdot \omega_m \quad (4.3.3)$$

The voltage loss due to commutation is current dependent. But for the linearization a mean current $\bar{I_d}$ of 2.4 A was used, which corresponds to half of rated generator current. It is done to have a simpler transfer function of the linearization and the fault by doing so is acceptable, as will be seen.

By applying Laplace transformation on the circuit elements the transfer function of the system can be found as Z_{eq}:

$$Z_{eq} = L_{eq}s + R_{eq} + (\frac{1}{sC} || R_{conv}) = \frac{s^2 + s(\frac{1}{R_{conv}C} + \frac{R_{eq}}{L_{eq}}) + \frac{R_{eq}+R_{conv}}{L_{eq}CR_{conv}}}{\frac{s}{L_{eq}} + \frac{1}{R_{conv}CL_{eq}}} \quad (4.3.4)$$

Where C is the is the DC-link capacitance and R_{conv} reperesent the damping of the converter equivalent. R_{eq} and L_{eq} are the transformed generator inductance and resistance calculated above. By applying τ_g as the generator time constant $\frac{L_g}{R_g}$ and τ_C as the converter circuit time constant R_{conv}C the expression can be simplified to equation 4.3.5.

$$Z_{eq} = \frac{s^2 + s(\frac{1}{\tau_c} + \frac{1}{\tau_g}) + \frac{1}{\tau_c \tau_g} + \frac{1}{L_{eq}C}}{\frac{1}{L_{eq}}(s + \frac{1}{\tau_C})} = \frac{(s + \frac{1}{\tau_g})(s + \frac{1}{\tau_c}) + \frac{1}{L_{eq}C}}{\frac{1}{L_{eq}}(s + \frac{1}{\tau_C})} \quad (4.3.5)$$

The evaluation of the linearization is done in comparison with simulations without voltage build up, since this would be the case for a real converter and since the behaviour of the mechanical switch is higly unlinear. An example of simulation without build up is shown in figure 4.3.3.

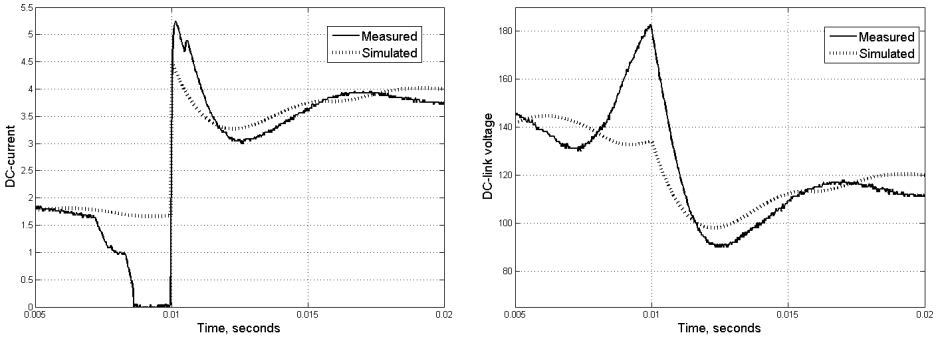

Figure 4.3.3: Measured and simulated step response without voltage build up.

It can be observed that the peak simulated current is approximately $0.8A$ lower than the peak measured current. And the transient appear a bit different. It is anyway plausible to assume that lab experiments with a semiconductor switch instead of a mechanical would coincide well with the simulated curve given the good results from the transient analysis.

The linearization and simulations are shown in figure 4.3.4- 4.3.7:

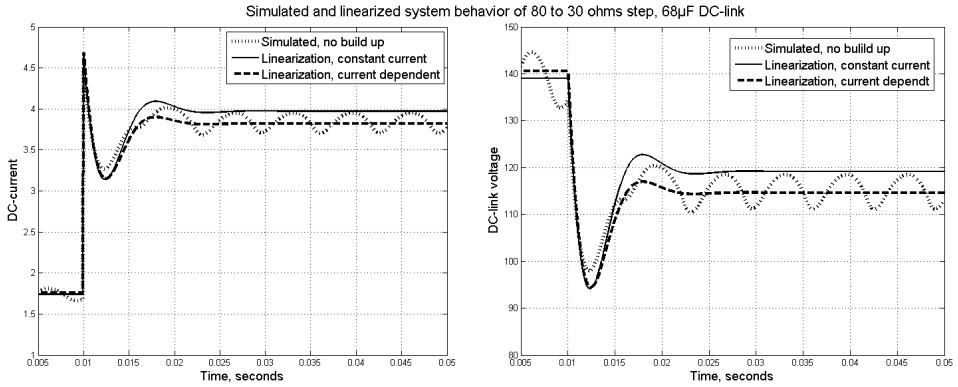

Figure 4.3.4: Linearization and simulation for 80 to 30 ohm step and 68 μF

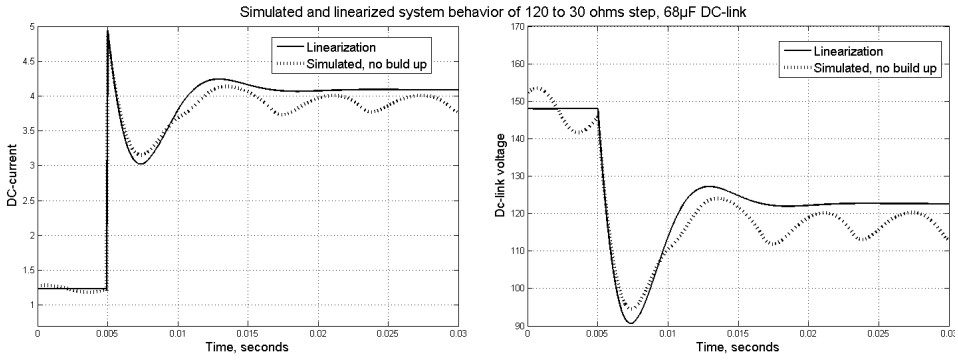

Figure 4.3.5: Linearization and simulation for 80 to 30 ohm step and 68 μF

The linearization concur well except for a small overshoot in the 68 μF tests, which may be caused by a higher steady state ripple for the $68\mu F$ series. The error done by assuming constant current dependence of the induced voltage is small, not more than 5 % as can be observed from the figures. Also it can be observed from figure 4.3.4, were a current dependent term is included in one simulation, that the steady state error is eliminated. If higher accuracy is needed it is possible to include a current dependent term in the estimation of the induced voltage by applying a current feedback loop. But as already mentioned, the transfer function will be more complicated. By looking at

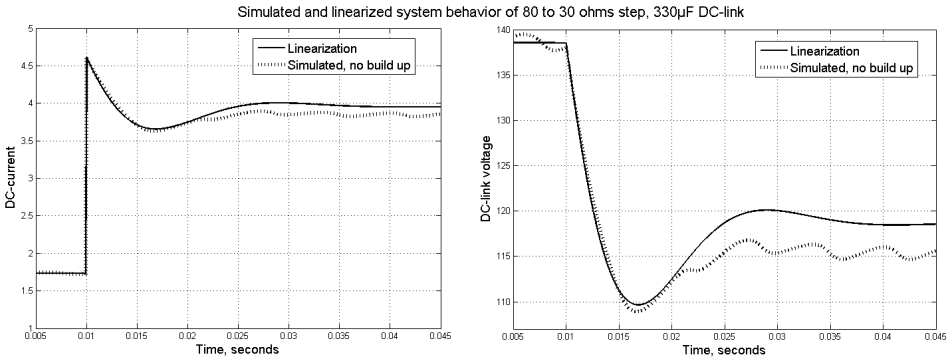

Figure 4.3.6: Linearization and simulation for 80 to 30 ohm step and 330 μF

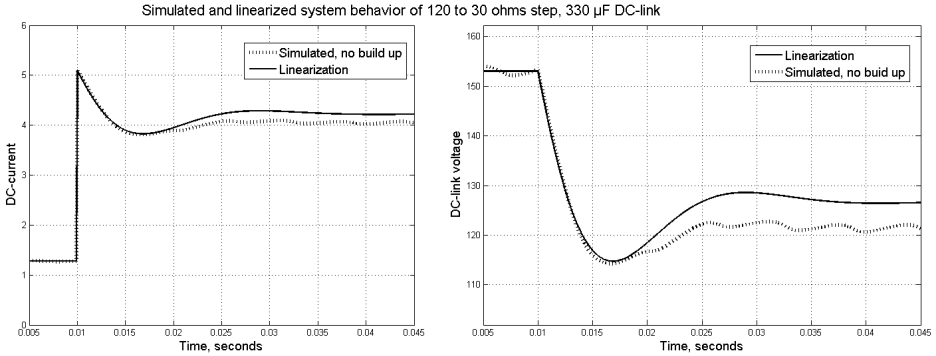

Figure 4.3.7: Linearization and simulation for 120 to 30 ohm step and 330 μF

step responses of the linearization is it possible to get more information about the system. A step in voltage is done and the corresponding current response is analyzed. By looking at current response also the force response of the system is examined because the quantities are proportional, equation 2.2.3. The current step response is presented in equation 4.3.6

$$I_{gen} = \frac{E_a}{Z_{eq}} = \frac{\frac{1}{s}}{\frac{(s+\frac{1}{\tau_g})(s+\frac{1}{\tau_c})+\frac{1}{L_g C}}{\frac{1}{L_g}(s+\frac{1}{\tau_C})}} = \frac{\frac{1}{L_g}(s+\frac{1}{\tau_C})}{s(s+\frac{1}{\tau_g})(s+\frac{1}{\tau_c})+\frac{1}{L_g C}} \tag{4.3.6}$$

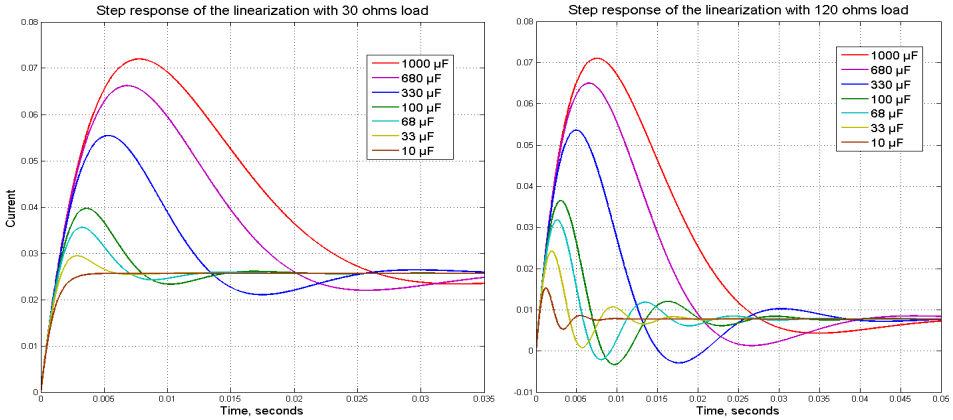

Figure 4.3.8: Step responses with largest and smallest damping and different capacitance.

Step responses with different capacitance at the DC-link is presented in figure 4.3.8.
The largest and smallest damping constants decided in chapter 3.4 is used i.e. 500 and 1500 $\frac{Ns}{m}$ and correspond to 30 ohms and 120 ohms converter resistance.

It can be observed that the step response for 330 μF is fairly slow and has a large overshoot, approximately 100 % and the choice of having a 330 μF DC-link capacitor in the project work simulations seems to be a bad decision. The overshoot become smaller as the capacitance is decreased and the response of the system improves and approaches a first order system response. Interpreted from the linearization step responses as little capacitance as possible would be the optimal for the system, but then it is important to remember that the model do not account for instability of the system due to high DC-link voltage ripple. This phenomenon will be investigated in the simulation chapter.

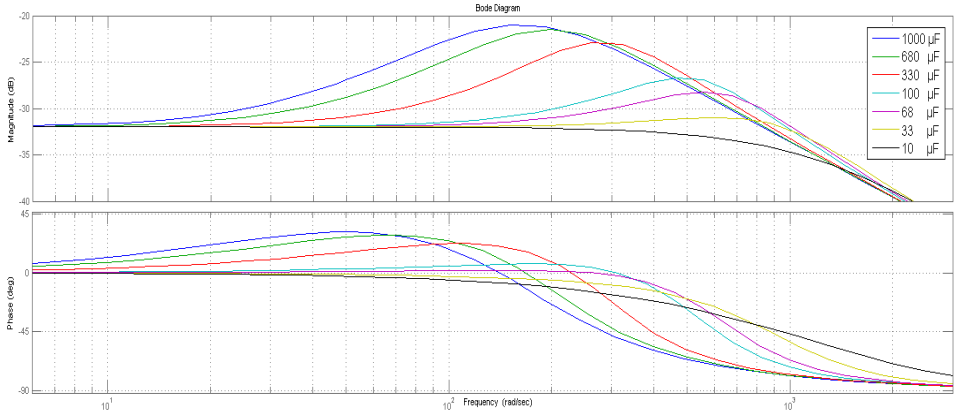

Figure 4.3.9: Bode plot for 30 ohm series, ferqency in $\frac{rad}{s}$

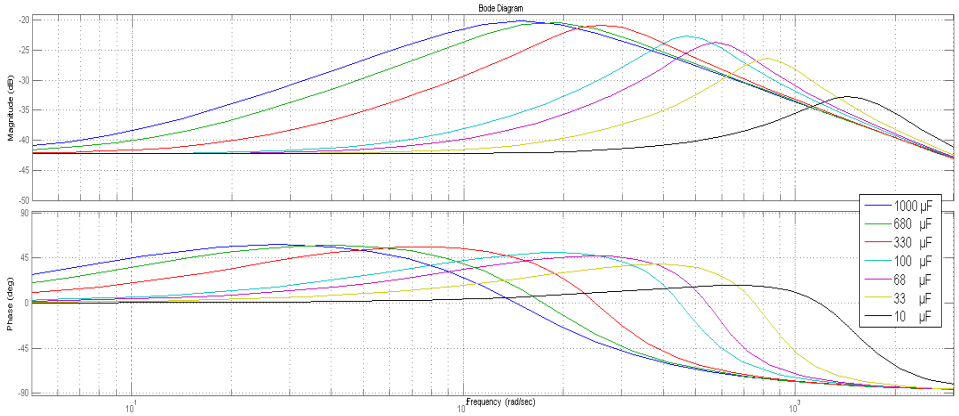

Figure 4.3.10: Bode plot for 120 ohm series, ferqency in $\frac{rad}{s}$

The bode diagrams for the the same capacitance and resistance is presented in figure 4.3.9 and 4.3.10
A resonance frequency can be observed in both plots which is plausible since the linearized model is a RLC circuit. It occur at lower frequencies as capacitance increases. The phase diagrams all end at $-90°$, which is likely because the capacitance acts like a short circuit at high ferquencies and resulting in a RL-circuit with current 90° lagging. 330, 68 and 10 μF DC-links will be applied in the simulation chapter and there preformance will be compared. Avoiding frequencies in the range of the resonance frequencies acting in the system is desirable. The approximate resonance frequencies is presented in table 4.3.1.

Capacitance	10 μF	68 μF	330 μF
Damping			
30 ohm / 1500 $\frac{Ns}{m}$	-	600 $\frac{rad}{s}$	300$\frac{rad}{s}$
120 ohm / 500 $\frac{Ns}{m}$	1500$\frac{rad}{s}$	600 $\frac{rad}{s}$	250 $\frac{rad}{s}$

Table 4.3.1: Approximate resonace frequencies for the selected DC-link capacitances in $\frac{rad}{s}$.

5 Simulations

5.1 Converter considerations

Selecting the right DC/DC converter for the system is an important task, but not easy. The project work concluded that a flyback converter would be a good choice, but a closer look at the selected converter indicated otherwise. A flyback converter has the advantage of very low parts count and is a good converter for small ratings usually 50-100 W. The drawback of a flyback converter is poor utilization of transformer core material. The flyback transformer is not a regular transformer but more like a two winding inductor since current do not flow in the two windings at the same time. It is called unipolar core excitation and implies that that no more than half of the inductor core materials B-H loop is utilized [8].The result is that a twice as big core is needed to transfer the same amount of energy in a flyback converter compared to a converter with bipolar core excitation. And as the rating increases the core of a flyback will be large because of this and lead to an uneconomical design.

Another solution that was looked at briefly was thyristor control. This turned out to be a bad idea because of problems with current commutation at low voltages. It has been observed that thyristors have problems with commutation if the voltage dip below 80 % of its nominal value [17]. For DC-link voltage control is a large span in voltage needed, and thyristor control is thus out of the question.

A plain boost converter was selected to be used in the simulations. The main reason was that such a converter is easy to implement in a lab set up with minimal work and construction. Standard 3-phase converters are easily available at campus and by using one leg of the converter is a boost inductor all that is needed of extra equipment in order to realize the design in the lab. Unfortunately was this not done because of lack of competence in converter control both with the author and at the institute of electrical power engineering. Learning the process of converter control from scratch was considered too time consuming.

5.2 Simulation with wave input

The simulations in this thesis are a continuance of the simulations in the project work. The same model is used, apart that the flyback converter is replaced with a step up converter for reasons mentioned above. Some of the parameters have also been changed to the once found in the lab experiments i.e. the generator resistance, inductance and voltage constant. Input to the simulations are samples of logged buoy position at the FO-rig during testing. By derivation of the position and filter it the speed of the buoy is

obtained and it can be put directly at the generator input, as shaft speed after multiplying with gear ratio. The speed input to the simulations are presented in figure 5.2.1.

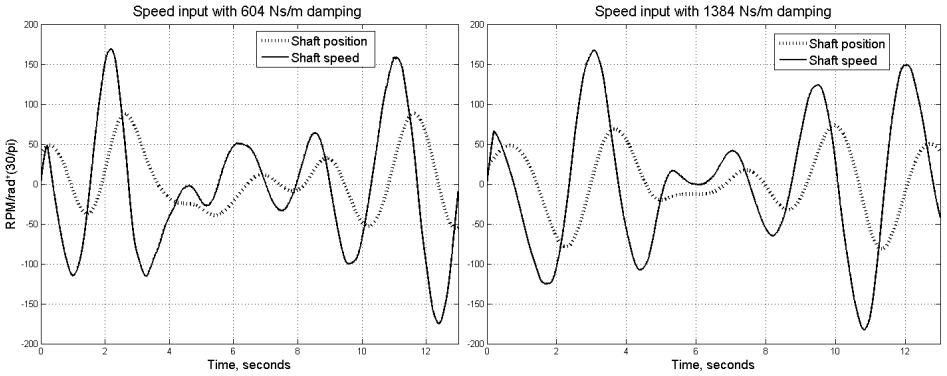

Figure 5.2.1: Logged bouy position and speed input to the simulation model.

The resulting speed from the wave input do not exceed 180 rpm at the shaft which implies that the generator is a bit oversized since the rated speed is 450 rpm. It was anyway useful to test the generator for speeds up to rated in the lab experiments if the generator is to be used for tests with rougher waves. The two test series are quite similar when it comes to wave amplitude and frequency so the same ripple frequency and amplitude at the rectified voltage can be assumed. The ripple frequency in the diode rectified voltage, ω_{ripp} ,is 6 times the electric frequency, $\omega_{electric}$. By using equation 2.2.6 the relation between ω_{ripp} and ω_{mech} in $\frac{rad}{s}$ is obtained:

$$\omega_{ripp} = 6 \cdot \omega_{electric} = 6 \cdot \frac{\pi}{30}\frac{p}{2}\omega_{mech} \approx 5 \cdot \omega_{mech} \tag{5.2.1}$$

The diode ripple frequency is thus varying in the range of 0-900 $\frac{rad}{s}$ in the simulation series.

The simulation model is shown in figure 5.2.2 and the simulation parameters in table 5.2.1.

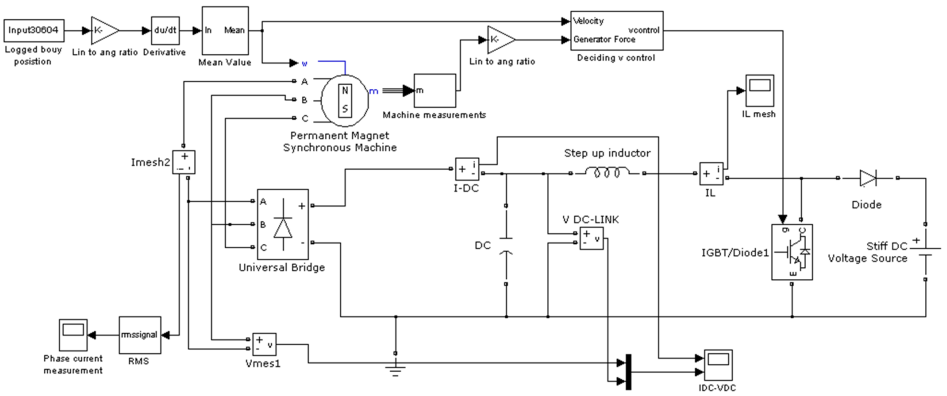

Figure 5.2.2: The SIMULINK model used as step up converter for real wave input.

Parameter	**Value**
D_{max}	0.8
D_{min}	0.2
Diode rectifier snubbers	R = 100 kohm, C = inf
Switch snubber	R = 5 kohm, C = inf
Regulator constants	$K_p = 5 \cdot 10^{-5}$ $K_i = 5 \cdot 10^{-2}$
Step up inductor	687.5 μH
Switching frequency	10 kHz
Gear ratio	28.05
DC-link capacitors	1 ,10,68 and 330 μF
Stiff DC voltage source	400 V
Damping constants	604 $\frac{Ns}{m}$ and 1384 $\frac{Ns}{m}$

Table 5.2.1: Simulation parameters

Maximum duty ratio is selected at max 0.8 to avoid effects of parasitic elements as discussed in chapter 2.3. A lower limit of 0.2 was also set, however there were no problems during simulations of the duty cycle exceeding its limits with the listed values. Snubbers where selected to influence the simulations as little as possible. The values were set by using a MATLAB/SimPowerSystems help file. The regulator constants, inductor inductance and switching frequency are the same as calculated in the project work. The inductance is the magnetizing inductance of the flyback converter calculated. Gear ratio is from the FO-rig. The capacitor values were the one used in the transient analysis 330 μF and 68 μF in addition

to 10 μF which indicated good response in the linear analysis. Based on the linearization an interesting task was to see if converter operation was improved by lowering the DC-link capacitance. The 1 μF capacitor used was to demonstrate unstable behaviour of the system as the DC-link capacitance became too small. The stiff voltage was set to a suitable point of 400 V. It was desirable to have the same damping constants in the simulations as in the lab experiments and the linearization i.e. 500 $\frac{Ns}{m}$ and 1500 $\frac{Ns}{m}$, but no suitable tests from the FO-rig existed. 604 $\frac{Ns}{m}$ and 1384 $\frac{Ns}{m}$ were the nearest once found which was fairly close.

A quasi block diagram is presented to give understanding of such system. In figure 5.2.3 is the mechanical part also included.

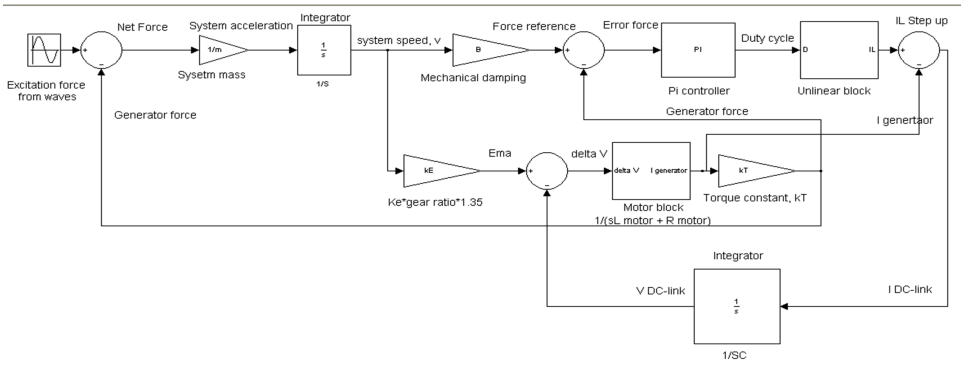

Figure 5.2.3: Blockdiagram of the system with mechanical system included.

The excitation force from the waves and the generator counter force give the total force acting on the point absorber. System acceleration is given depending on system mass. The speed dictates both force reference i.e. passive loading, and the induced voltage of the generator. By subtracting the actual generator force from the reference is the force error given. This covers the mechanical part of the system. The sum of currents in the DC-link point is zero thus is the difference in generator current and inductor current equal the DC-link current,see figure 5.2.2. Integration of DC-link current give the DC-link voltage with a factor of $\frac{1}{C}$. The difference in induced voltage and DC-link voltage together with the generator impedance decides the generator current and thus the generator force. The error in force is fed into a PI-regulator and decides duty cycle of the converter and thus inductor current. This is how the generator force indirectly is controlled by changing the duty cycle. For the simulations in this work the mechanical part of the system is excluded by applying measured speed at the generator input and the generator force feedback loop in figure 5.2.3 is let out as shown in figure 5.2.4.

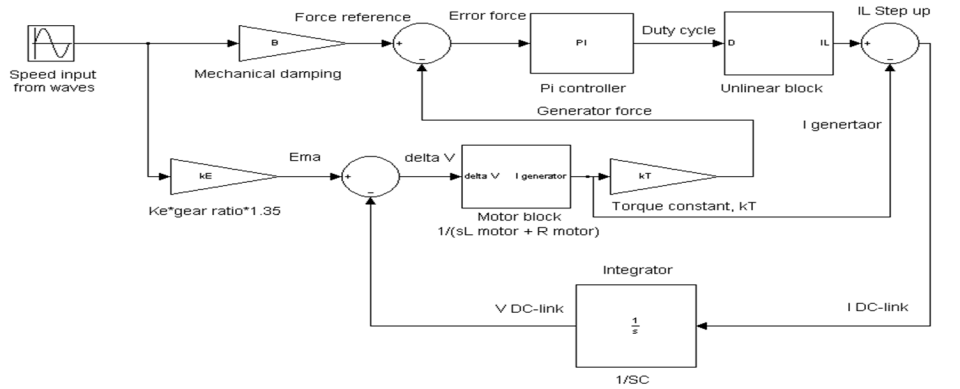

Figure 5.2.4: Blockdiagram of the system as used in simulations.

By using the same damping constant in the simulations as used during the tests the behaviour of the force feedback loop will be emulated and hopefully give authentic simulations. This is because the generator force both from the from the test and simulations become the same with equal damping constant, B_{damp}.
The results from the simulations are presented in figure 5.2.5 to 5.2.7:

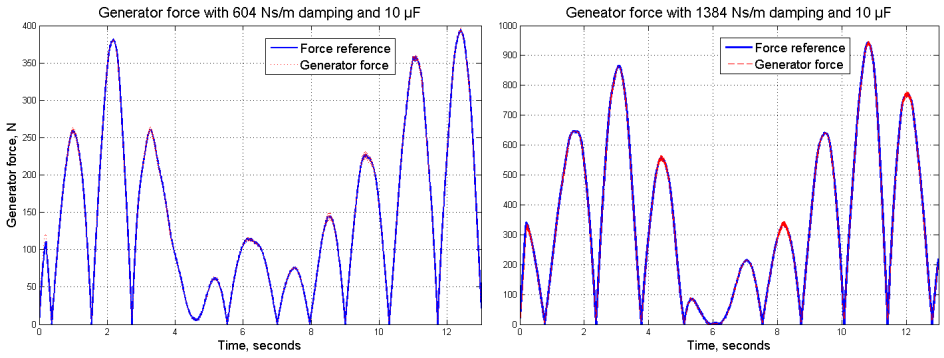

Figure 5.2.5: Force and reference with 10 μF.

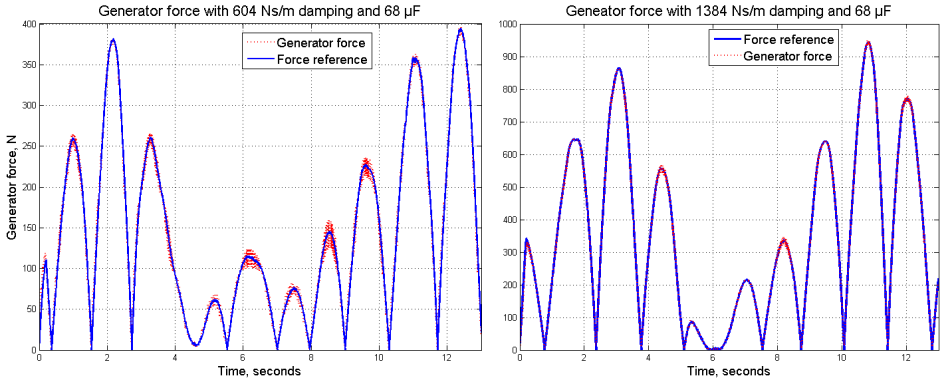

Figure 5.2.6: Force and reference with 68 μF.

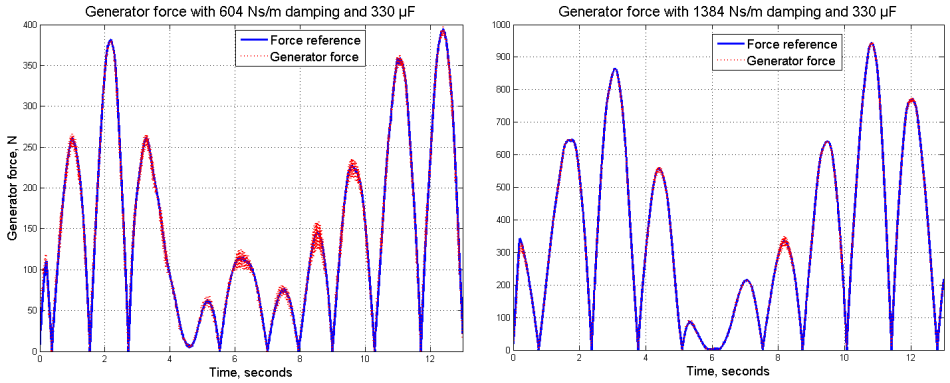

Figure 5.2.7: Force and reference with 330 μF.

All series show stabile behavior and follows the reference value with both wave inputs. The simulated torque is taken the mean value of over a period 0.03 seconds this to easily be able to compare the actual torque with the reference value. Ripple in the tests will be compared for DC-current which is almost the same as comparing torque ripple because of propotionality. Some ripple can still be observed in the 604 $\frac{Ns}{m}$ series.

DC-side current is presented in figure 5.2.9.

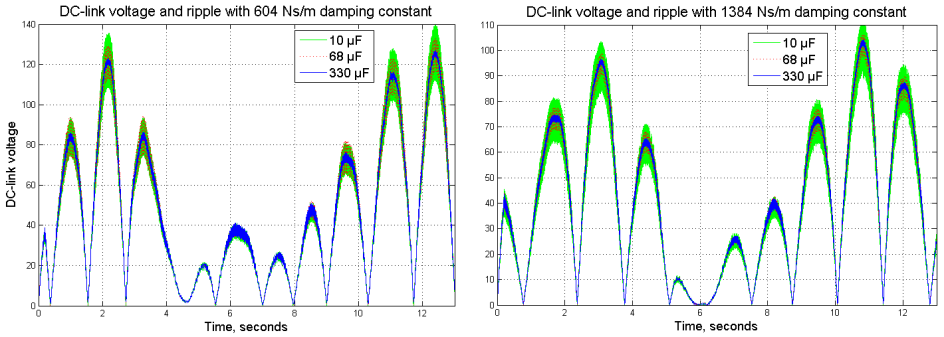

Figure 5.2.8: DC-link voltage for both test series and the 3 DC-link capacitances.

DC-link ripple is as expected mostly largest for 10 μF. Current is the same and less capacitance thus give larger ripple as can be seen in equation 2.3.2. There are some exceptions as for 330 μF at low speeds in the 604 $\frac{Ns}{m}$ series that will be explained later. DC-side current is presented in figure 5.2.9.

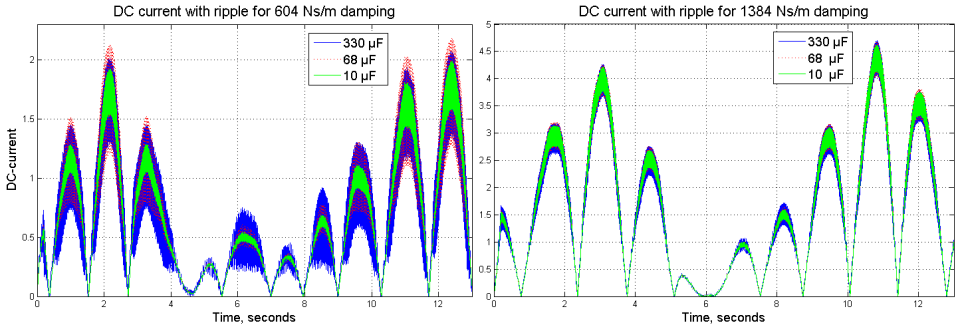

Figure 5.2.9: Generator current at the DC-side

The larger current ripple in the 604 $\frac{Ns}{m}$ series may be explained by the higher amplitude of the resonance frequency in the bode plot in figure 4.3.10. Largest ripple alternate between the 330 μF and 68 μF series throughout the test. Especially high ripple can be observed in the 330 μF at 6 seconds. Speed of the generator at that instance is 50 rpm which give a ω_{ripp} of 250 $\frac{rad}{s}$, from equation 5.2.1 that coincide with the resonance frequency in table 4.3.1. Speed ripple for the 604 $\frac{Ns}{m}$ series at speed peaks are summarized in table 5.2.2.

Peak instant, s	speed, ω_{mech}	Largest ripple series, μF	ω_{ripp}	$\omega_{resonance}$
1.0	115	68	575	600
2.2	168	68	840	600
3.3	115	68	575	600
6.2	50	330	250	250
8.5	65	330	325	250
9.6	100	330	500	250
11.0	160	68	800	600
12.4	175	68	875	600

Table 5.2.2: Current ripple at speed peaks

The results are not consistent, but indicate a strong relation between current ripple and the concurrence of the two frequencies ω_{ripple} and $\omega_{resonance}$, which is reasonable. This is strengthen by the fact that ripple for the 10 μF series is smallest at all times; its resonance frequency, 1500 $\frac{rad}{s}$, is larger than the maximum ω_{ripple}, of 900 $\frac{rad}{s}$ hence is ripple minimized. For the DC-link ripple exception earlier mentioned it can be explained by the ripple frequency approaching the resonance frequency. The duty cycle of the converter is presented in figure 5.2.10.

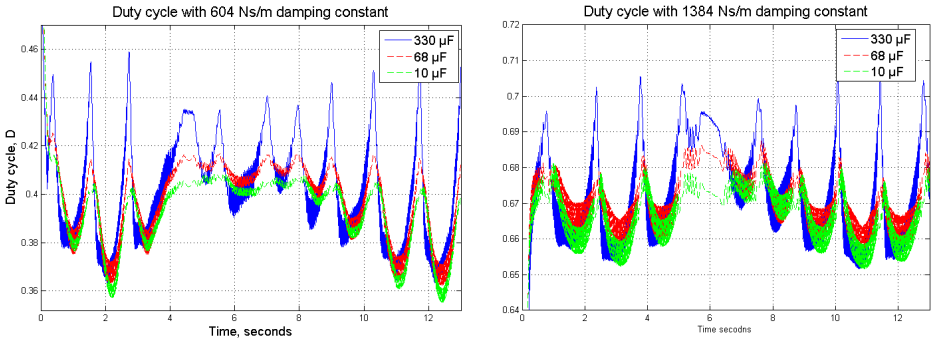

Figure 5.2.10: Duty cycle, of all the series.

The same pattern of ripple also can be observed in the duty cycle of the simulations. The 330 μF has the largest span in duty cycle and the 10 μF has the least. Little span in duty cycle is an advantage when it comes to controlling the converter, also it is easier to make a linearization of the converter it self. Inductor current is presented in figure 5.2.11.

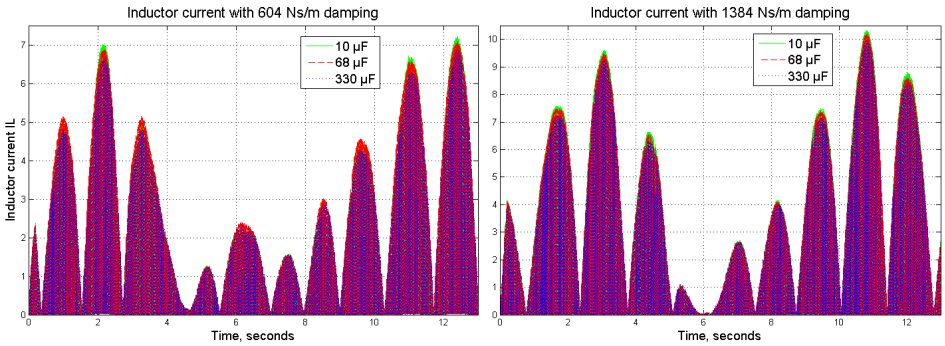

Figure 5.2.11: Inductor current for both test series and the 3 DC-link capacitances.

Peak inductor current is also the peak switch current and the switch need to dimensioned to carry that current. A large mean to peak ratio can be observed by comparing the inductor current with the DC-current and the converter is working in DCM. This is not desirable because the rating of the switch and thus the cost of it is increased. The largest cost of a converter is often the active semiconductors and good utilization of the switch is important for making a cost-effective design [8]. By lowering the stiff DC-voltage the maximum switch current can be reduced some. Another way to lower the peak current is by increasing the inductance of the boost inductor. This was tried for the actual converter, but it caused the duty cycle to reach its upper limit of 0.8 and instability was experienced as the inductance was increased. This phenomenon should be investigated for further work. In figure 5.2.12 unstable behaviour caused by insufficient DC-link capacitance, can be observed.

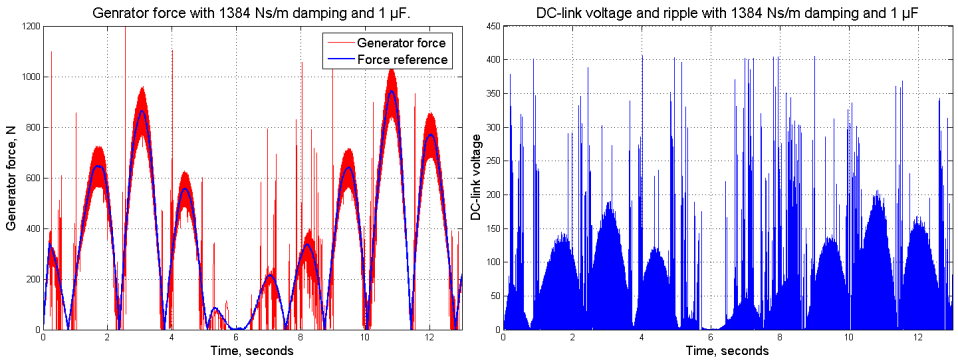

Figure 5.2.12: Unstable control because caused by insufficient DC-link capacitance.

6 Discussion

The problem experienced with torque ripple in the project work is largely reduced due to higher generator phase inductance than assumed. Phase inductance used in the project simulations was 1 mH and during the lab experiments in this work has phase inductance been estimated to 23.9 mH. One of the main tasks for further work from the project was to investigate the consequences of the torque ripple both for short time vibrations during operation and long term fatigue due to the fluctuations. No vibrations influencing the system due to torque fluctuations were experience during the laboratory work. The torque fluctuations experienced in the simulations should not contribute to stresses influencing the lifetime of the WEC. If it turns out it will additional inductance at the DC-side can be applied to smoothen the torque to an acceptable level. The trade off by doing so is additional cost of the system.

As demonstrated in simulations the linearization can be used to reduce torque ripple by interpreting the behaviour of the linearization step responses and bode plots. The linearization was then used to identify resonance frequencies of the system and avoiding them to coincide with voltage ripple caused by the diode rectifier. The same probably apply for the switching frequency of the converter, but it did not interfere in this particular case since it was significantly higher the resonance frequencies.

The linearization model has indentified the key parameters for the investigated system and the result is a generalized model. If the generator phase inductance, resistance and voltage constant in addition to desired damping is known. The linearization in combination with stability simulations of the converter can be used to calculate the optimal DC-link capacitance. The model also can be helpful when selecting permanent magnet generator for a wave energy converter of this type. Time delay associated with generator and converter system also can be determined by using the model. This is useful in stability studies of the entire WEC. The system responses experienced in the transient analysis represents a time delay of 10 - 20 ms from the PTO force reference to PTO force, depending on the DC-link capacitance. It is indicated from the FO3-project that a time delays off less than 50 ms is manageable. However the response was tested on a small scale device which in itself is not very interesting, the interesting part is that the model is generalized and can be applied at a commercial size WEC.

On the other hand the model has its limitations; it only can be applied for passive loading control. Other strategies for controlling power output from the WEC are in the continuation interesting to look at. Freewheeling and latching are control strategies were damping is changed during operation.

The model cannot be adapted to these control strategies. Acceleration phase control is also a possible control strategy, a force proportional to the acceleration of the system is then applied. It should be possible to implement acceleration control in the model by using the same analogy as for damping constant B and resistance R. By changing speed with acceleration and voltage by derivated voltage, an acceleration constant, A, is inversely proportional to a Capacitance, c. However acceleration control of the investigated system would probably be difficult because acceleration is mainly largest at zero speed and the generator cannot supply any current when speed is 0. The generator of the model could also be changed to for instance an induction generator if it is desirable. An induction generator circuit model is a bit more complicated to implement than a PMG, but the task should be fairly manageable. The converter in the model is general and the choice of DC-DC-converter can be chosen freely as long as it emulates passive loading. A more detailed converter model is difficult to make since the converter is working both in CCM and DCM and the duty cycle is changing constantly. The reduction in ripple experienced in simulations minimized the span of D and should make it easier to represent the converter with a state-space model.

The good results from the steady state and dynamic input analysis imply that the simulation model can be up scaled and applied for simulating a commercial size device. In addition components used in the converter during simulations were few and with relatively small ratings. One switch was used instead of six which had been the case for a back to back converter. This may indicate that the selected converter type is cheaper than a regular back to back converter.

Further work

Applying the linearization model to a commercial size system in order to do an analysis of it is very interesting and is the natural next step. This will be done in cooperation with Fred Olsen during summer 2009. For further experimental work a converter should be implemented in a lab set up to verify that the suggested control is possible. A detailed converter analysis should be done in advance. The selected converter could for instance be represented with a state-space model. For further simulations could other control strategies be implemented in the existing simulation model e.g. acceleration control. In this work it was assumed that the selected system was cheaper than a back to back converter. This should be investigated by doing a quantitative economical analysis of the system to find out if this is the case.

7 Conclusion

In this work a wave energy converter with direct electric drive as power take off and passive loading as control strategy has been investigated both with experimental work and with simulations. The generator used was a permanent magnet type which is suited for wave energy conversion due to high pole number. The converter system used included a diode rectifier, a DC-link and a step up converter and was assumed cheaper than a regular back to back converter.

In the lab experiments were the converter represented by different resistors corresponding to desired damping values. Three different lab series were done: A steady state analysis, an analysis with dynamic input representing waves and a transient analysis. A simulation model was verified on basis of results obtained in the lab. The steady state simulations had very good accuracy for voltage and current, mainly under $\pm$ 1 % deviation compared to the measured values. For torque were the deviations between measured and simulated values higher. This could be expected since the simulation model did not account for mechanical loss in torque. The torque simulations still gave a good indication of the measured torque and deviations were mostly in the range of $\pm$ 8 %. Similar precision was obtained for the dynamic input analysis, mostly a in the range of $\pm$ 3 % for voltage and current and $\pm$ 5 % for torque. Transient measurements and simulations also concurred well and a linearization based on the results was made.

In simulations a step up converter with switching was included. Wave data from the FO-rig was used as input to the model and stable control was emulated with passive loading. In order to improve the response of the simulation model the linearization transfer function was used to interpret the behaviour of the system by examine step responses and bode plots. The results indicated that by decreasing the DC-link capacitance could the response of the simulation model be improved. This proved to be true and it resulted in less torque ripple by avoiding resonance frequencies to coincide with ripple frequencies. The linearization also can be used to identify the time delay of the power take off device in a wave energy converter, which is of particular interest when designing a WEC.

References

[1] International energy agency report *"Key issues in developing renewables"*, 1997.

[2] Pelamis press release: $http://www.pelamiswave.com/news.php?id=26\&categoryId=3$

[3] Molinas, M.; Skjervheim, O.; et al. *"Power electronics as grid interface for actively controlled wave energy converters."*

[4] Muetze, J. and Vining, J.G. *"Ocean wave energy conversion - A Survey."*

[5] Xiang, J.; Brooking, P. R. M. and Mueeller, M. A, *"Control requriements of Direct electric wave energy converters."*

[6] Mohan, N.; Undeland, T. M. and Robbins, W. P. *"Power electronics, converters, applications and design."*, Wiley 2003.

[7] Nilsen, R. compendium in *"TET 4120 Elektriske motordrifter"*, 2005.

[8] Erickson, R.W.; Maksimovic, D. *"Fundamentals of Power Electronics"*, second edition, Kluwer academic publisher 2001.

[9] Eltamaly, A. M. *"Modeling of wind turbine driving permanent magnet generator with maximum power point tracking system."*

[10] Vergauwe, J. et al. *"Optimization of a wind turbine using permanent magnet synchrounous generator(PMSG)."*

[11] Manual for fluke 112 multimeter, ftp://ftp.testequity.com/pdf/110series.pdf

[12] Kim, S.H.; Doose, C. *"Temperature compensation of NdFeB permanent magnets"*

[13] Properties of NdFeB magnets, http://www.magnetsales.com/Neo/Neoprops.htm

[14] HBM MP 55 Manual http://www.hbm.com.pl/pdf/a0563.pdf

[15] Mohan, N. *"Electric drives, an integrative approach"*, Mnpere 2003.

[16] Mohan, N. *"Advanced electric drives"*, Mnpere 2001.

[17] Roberton, R. A.; Børnes, A. H. *"Adjustable-Frequency Drive System for North Sea Gas Pipeline."*

[18] Balchen, J.G.; Andresen, T.; Foss, B.A. *"Reguleringsteknikk"*, Institutt for teknisk kybernetikk, NTNU, 2003.

[19] Nilsson, J.W.; Riedel, S.A. *"Electric circuits"*, seventh edition, Prentice Hall, 2005.

Appendices

A Dynamic analysis results

The figures for the rest of the dynamic analysis are given in here:

A.1 120 ohms load

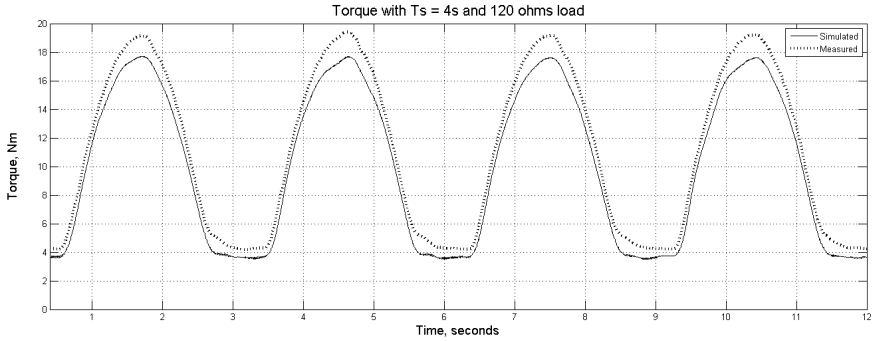

Figure A.1.1: Measured and simulated torque 120 ohms and four seconds wave period.

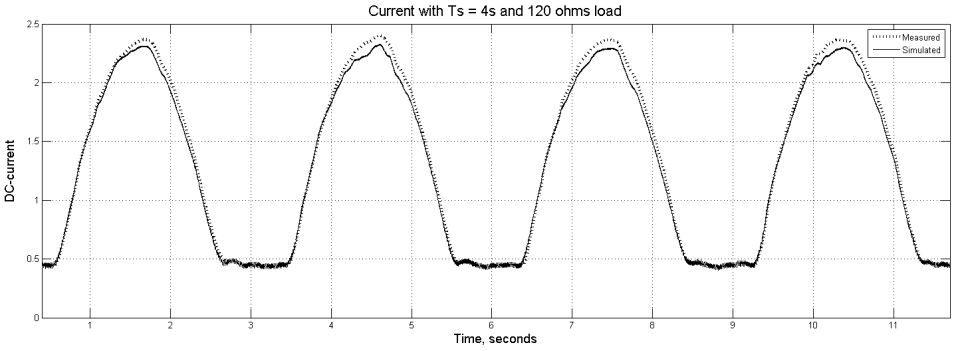

Figure A.1.2: Measured and simulated current 120 ohms and four seconds wave period.

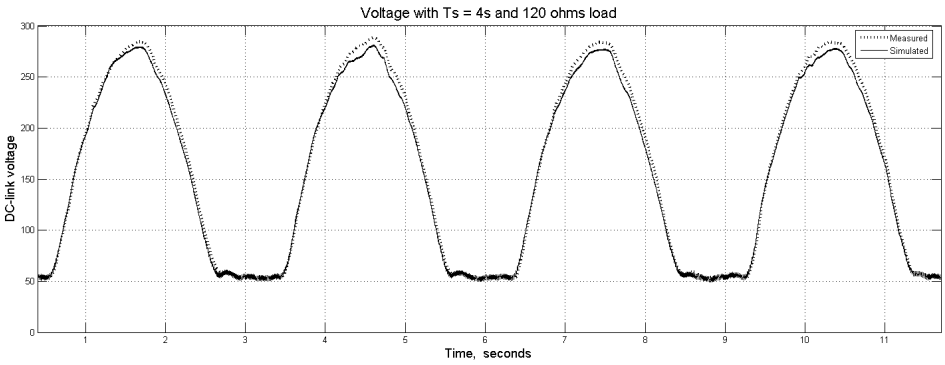

Figure A.1.3: Measured and simulated voltage 120 ohms and four seconds wave period.

A.2 80 ohms load

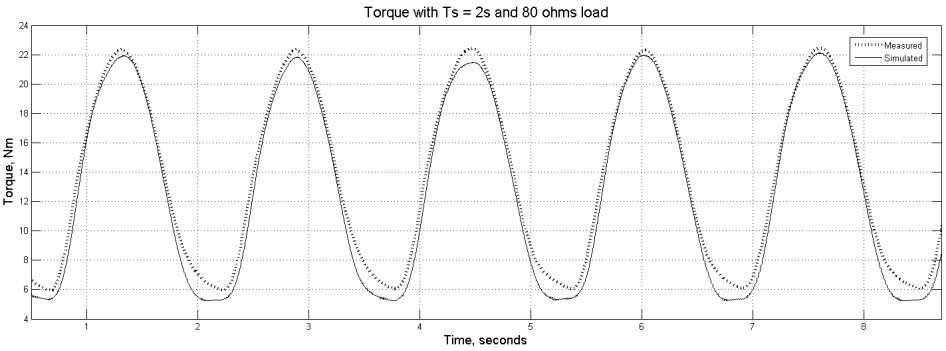

Figure A.2.1: Measured and simulated torque 80 ohms and two seconds wave period.

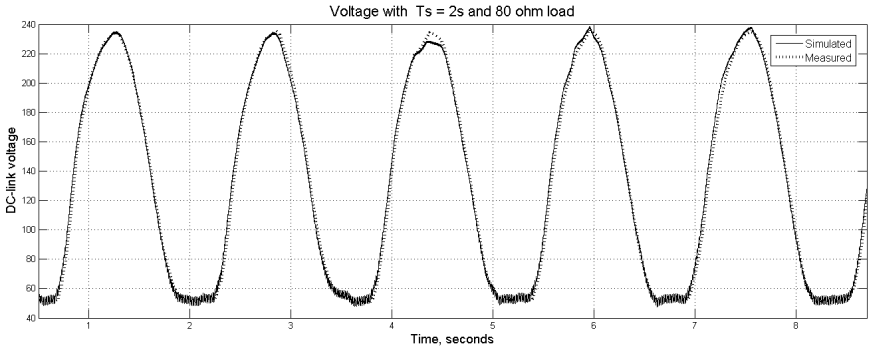

Figure A.2.2: Measured and simulated voltage 80 ohms and two seconds wave period.

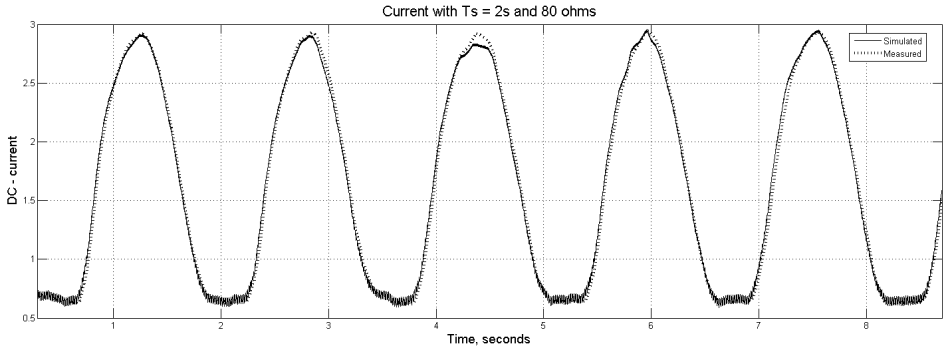

Figure A.2.3: Measured and simulated current 80 ohms and two seconds wave period.

A.3 50 ohms load

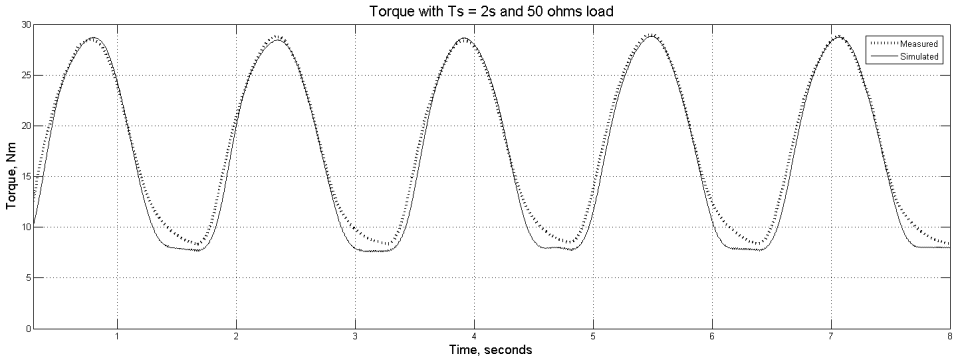

Figure A.3.1: Measured and simulated torque 50 ohms and two seconds wave period.

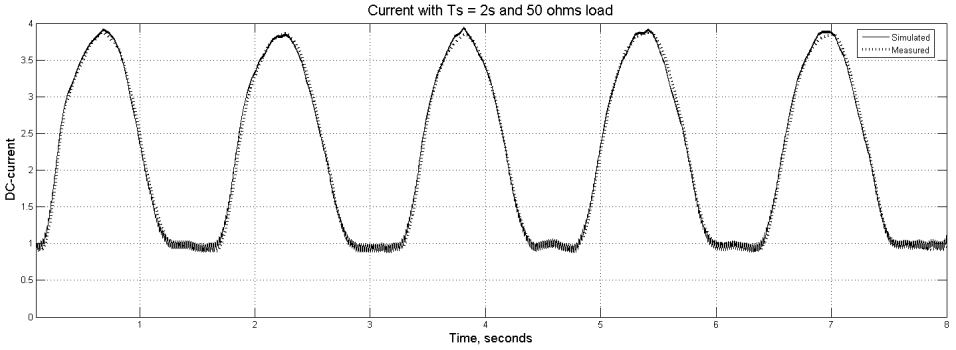

Figure A.3.2: Measured and simulated current 50 ohms and two seconds wave period.

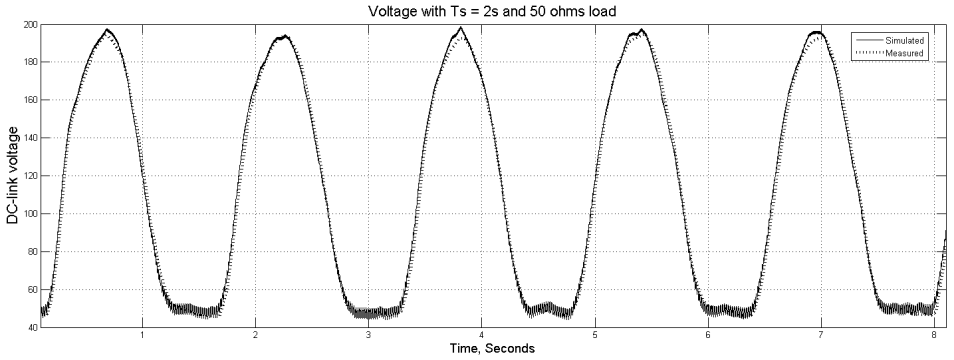

Figure A.3.3: Measured and simulated voltage 50 ohms and two seconds wave period.

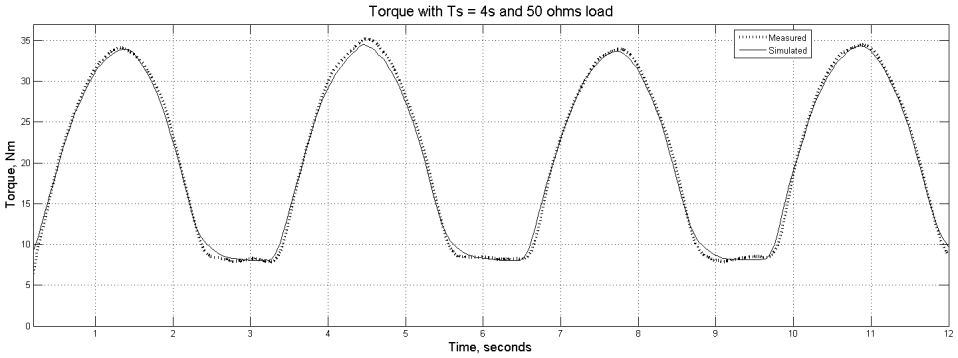

Figure A.3.4: Measured and simulated torque 50 ohms and four seconds wave period.

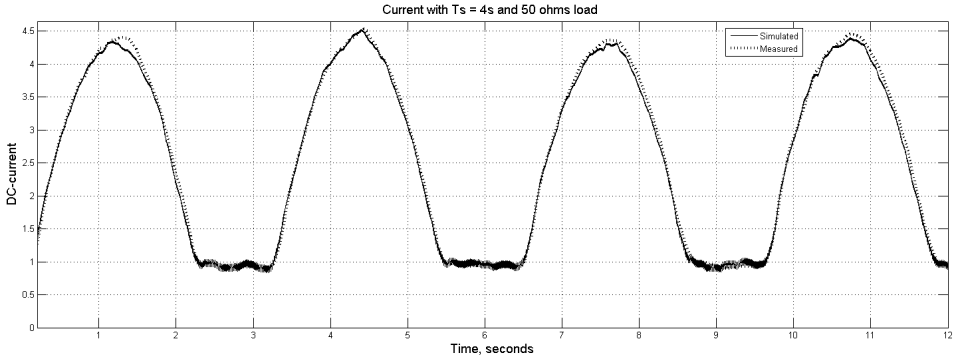

Figure A.3.5: Measured and simulated current 50 ohms and four seconds wave period.

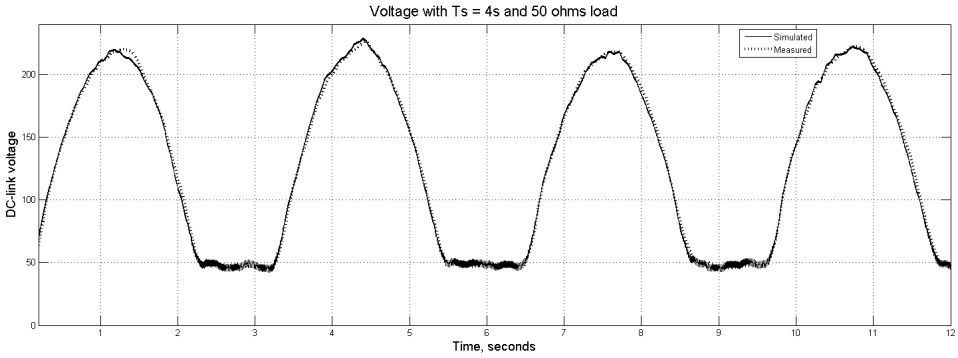

Figure A.3.6: Measured and simulated voltage 50 ohms and four seconds wave period.

A.4 30 ohms load

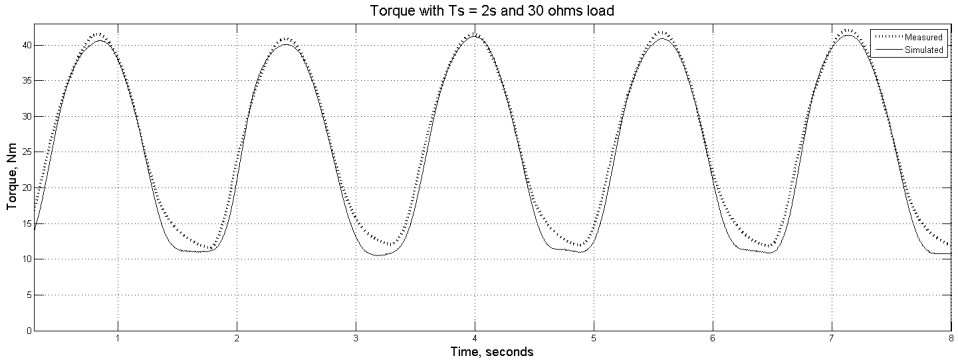

Figure A.4.1: Measured and simulated torque 30 ohms and two seconds wave period.

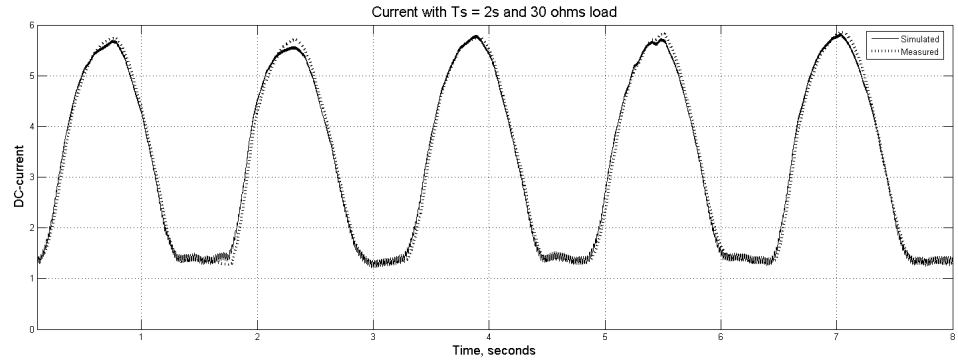

Figure A.4.2: Measured and simulated current 30 ohms and two seconds wave period.

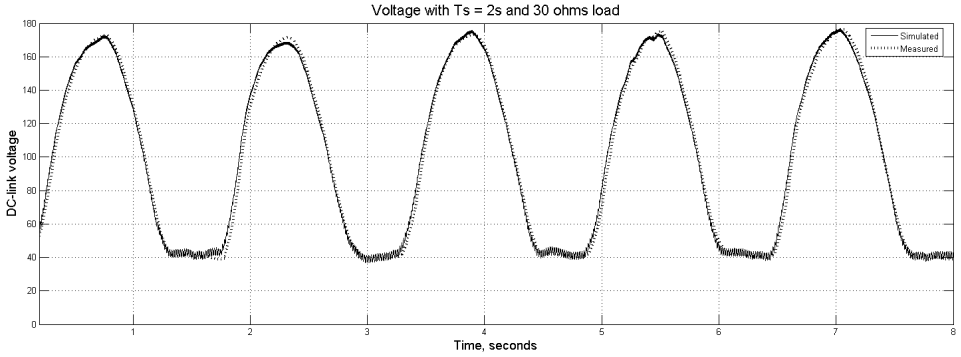

Figure A.4.3: Measured and simulated voltage 30 ohms and two seconds wave period.

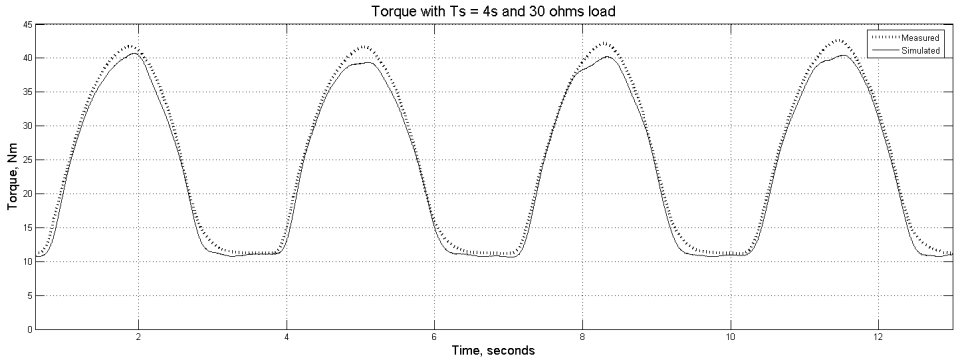

Figure A.4.4: Measured and simulated torque 30 ohms and four seconds wave period.

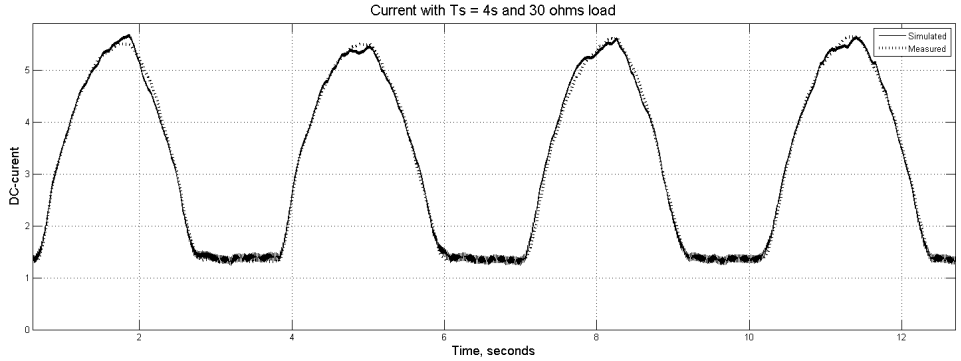

Figure A.4.5: Measured and simulated current 30 ohms and four seconds wave period.

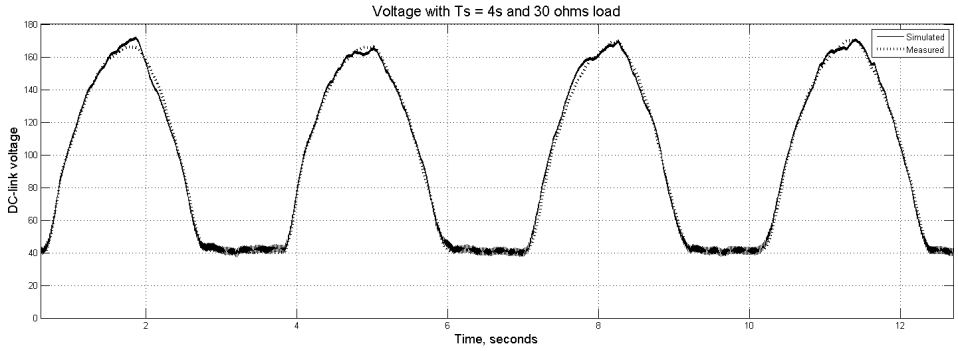

Figure A.4.6: Measured and simulated voltage 30 ohms and four seconds wave period.

B Generator documentation

The generator documentation given is presented in figure B.1. In table B.1, is the calculated values based on the expermental work done presented.

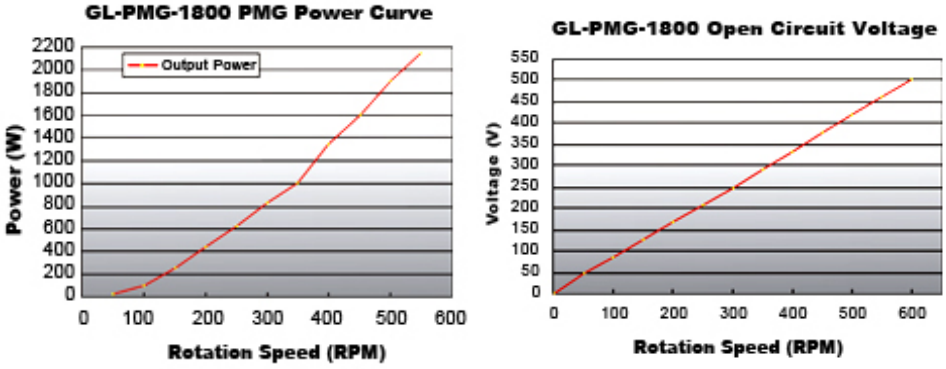

Figure B.1: Permanent magnet generator induced voltage and power.

Generator parameter	Value
Phase resistance	4.9 ohm
Phase inductance	23.9 mH
polenumer	16
kE	$0.885\frac{V_{LL-peak}}{rpm}$
Nominal phase current	3.9 A
Nominal speed	450 rpm

Table B.1: Permanent magnet generator constants.

C Wave climate at FO-rig Løkstad

Typical wave data from Løkstad is shown in figure C

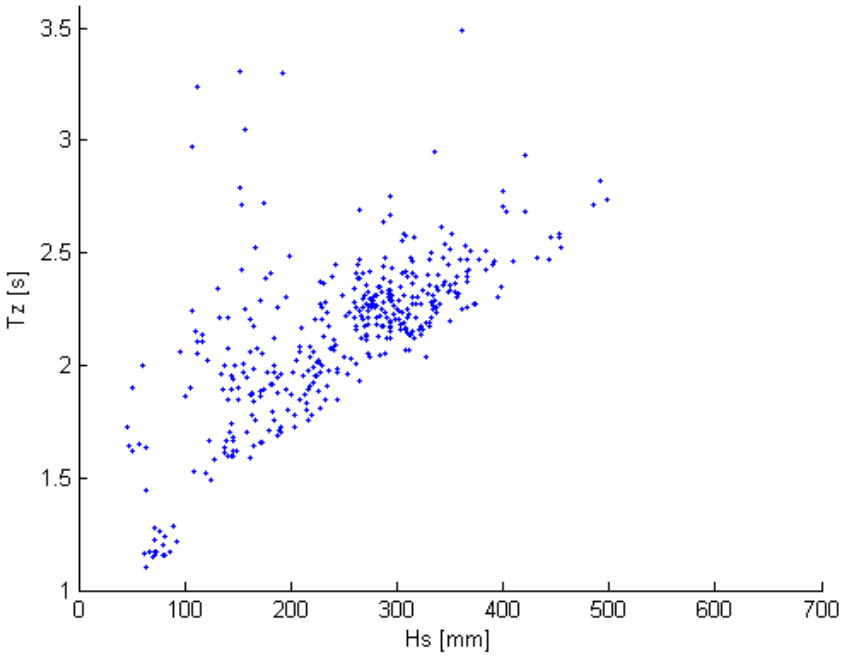

Figure C.1: Scatterplot of typical wave climates at Løkstad test station.